

**METALLOPORPHYRIN-SENSITIZED  
TITANIA/SILICA/IRON OXIDE NANOCOMPOSITES AND  
THEIR PHOTOCATALYTIC ACTIVITIES**

**Miss Padtaraporn Chanhom**



A Dissertation Submitted in Partial Fulfillment of the Requirements  
for the Degree of Doctor of Philosophy in Chemistry  
Department of Chemistry  
Faculty of Science  
Chulalongkorn University  
Academic Year 2018  
Copyright of Chulalongkorn University

นาโนคอมพอสิตของไททานี/ซิลิกา/เหล็กออกไซด์ที่มีเมทัลโลพอร์ไฟรินไวแสงและกัมมันต  
ภาพการเร่งปฏิกิริยาด้วยแสง



วิทยานิพนธ์นี้เป็นส่วนหนึ่งของการศึกษาตามหลักสูตรปริญญาวิทยาศาสตรดุษฎีบัณฑิต  
สาขาวิชาเคมี ภาควิชาเคมี  
คณะวิทยาศาสตร์ จุฬาลงกรณ์มหาวิทยาลัย  
ปีการศึกษา 2561  
ลิขสิทธิ์ของจุฬาลงกรณ์มหาวิทยาลัย

Thesis Title METALLOPORPHYRIN-SENSITIZED  
TITANIA/SILICA/IRON OXIDE  
NANOCOMPOSITES AND THEIR  
PHOTOCATALYTIC ACTIVITIES  
By Miss Padtaraporn Chanhom  
Field of Study Chemistry  
Thesis Advisor Assistant Professor Numpon Insin, Ph.D.

---

Accepted by the Faculty of Science, Chulalongkorn University in Partial  
Fulfillment of the Requirement for the Doctor of Philosophy

..... Dean of the Faculty of Science  
(Professor POLKIT SANGVANICH, Ph.D.)

DISSERTATION COMMITTEE

..... Chairman  
(Associate Professor VUDHICHAJ PARASUK, Ph.D.)  
..... Thesis Advisor  
(Assistant Professor Numpon Insin, Ph.D.)  
..... Examiner  
(Associate Professor KHANITHA PUDHOM, Ph.D.)  
..... Examiner  
(WIPARK ANUTRASAKDA, Ph.D.)  
..... External Examiner  
(Nisanart Charoenlap, Ph.D.)

จุฬาลงกรณ์มหาวิทยาลัย  
CHULALONGKORN UNIVERSITY

ภัทรภรณ์ จันทร์หอม : นาโนคอมพอสิตของไททานีย/ซิลิกา/เหล็กออกไซด์ที่มี  
เมทัลโลพอร์ไฟรินไวแสงและกัมมันตภาพการเร่งปฏิกิริยาด้วยแสง. (

**METALLOPORPHYRIN-SENSITIZED  
TITANIA/SILICA/IRON OXIDE  
NANOCOMPOSITES AND THEIR  
PHOTOCATALYTIC ACTIVITIES)** อ.ที่ปรึกษาหลัก : ผศ.

ดร.นำพล อินสิน

การสังเคราะห์นาโนคอมพอสิตของไททานีย-ซิลิกา-เหล็กออกไซด์ เป็นตัวเร่งปฏิกิริยาที่มีสมบัติการตอบสนองแม่เหล็กซึ่งสามารถถูกกระตุ้นด้วยแสงในช่วงที่ตามองเห็นได้ด้วยการเพิ่มโมเลกุลเมทัลโลพอร์ไฟรินบนพื้นผิวของคอมพอสิต โดยทำการศึกษาความแตกต่างของชนิดโลหะที่อยู่ในเมทัลโลพอร์ไฟรินต่อผลของการสลายสีของเมทิลีนบลูภายใต้การฉายแสงจากหลอดไส้เป็นเวลาสามชั่วโมง คอมพอสิตที่สังเคราะห์ได้ถูกพิสูจน์เอกลักษณ์ด้วยเทคนิคอัลตราไวโอเลต-วิสิเบิล สเปกโทรโฟโตเมตรี, เอกซเรย์ดิฟแฟร็กโทเมตรี, ฟลูออโรสเปกโตรสโกปีอินฟราเรดสเปกโทรสโกปี, และเอกซเรย์โฟโตอิเล็กตรอนสเปกโทรสโกปี จากผลการย่อยสลายเมทิลบลู พบว่าการมีเมทัลโลพอร์ไฟรินบนพื้นผิวของคอมพอสิต สามารถช่วยให้คอมพอสิตของไททานีย-ซิลิกา-เหล็กออกไซด์ดูดกลืนแสงในช่วงที่ตามองเห็นได้ คอมพอสิตของไททานีย-ซิลิกา-เหล็กออกไซด์กับเมทัลโลพอร์ไฟรินที่มีทองแดงอยู่ในโครงสร้าง สามารถกำจัดสีของเมทิลีนบลูและแบคทีเรีย *Escherichia coli* ได้ภายใต้การฉายแสงสามชั่วโมง คอมพอสิตดังกล่าวสามารถนำกลับมาใช้ซ้ำได้สี่ครั้ง โดยไม่ผ่านกระบวนการฟื้นฟูพื้นผิวใด ๆ แสดงให้เห็นว่าคอมพอสิตที่สังเคราะห์ได้นั้นมีประสิทธิภาพในการนำกลับมาใช้ซ้ำได้ดีด้วยการแยกโดยอาศัยแรงแม่เหล็กจากภายนอกมาเหนี่ยวนำ ประสิทธิภาพในการสลายสีของเมทิลีนบลูไม่เพียงขึ้นกับชนิดของโลหะในเมทัลโลพอร์ไฟริน แต่ยังขึ้นกับปริมาณพอร์ไฟรินที่ติดอยู่บนพื้นผิวของคอมพอสิตด้วย การให้ความร้อนที่ 60 องศาเซลเซียสพร้อมกับการปั่นกววน โดยใช้ 0.01 มิลลิโมลของ Copper(II) tetra(4-carboxyphenyl)porphyrin (CuTCPP) ต่อ 50 มิลลิกรัมของคอมพอสิตของไททานีย-ซิลิกา-เหล็กออกไซด์ คืออัตราส่วนที่เหมาะสมในการเตรียมคอมพอสิตให้มีประสิทธิภาพสูง คอมพอสิตที่ได้นี้มีประสิทธิภาพในการใช้เป็นตัวเร่งเชิงแสงได้ในงานที่หลากหลายต่อไป

จุฬาลงกรณ์มหาวิทยาลัย  
CHULALONGKORN UNIVERSITY

สาขาวิชา เคมี

ลายมือชื่อนิสิต

ปีการศึกษา 2561

ลายมือชื่อ อ.ที่ปรึกษาหลัก

# # 5772882023 : MAJOR CHEMISTRY

KEYWORD Titanium dioxide, Silica, Porphyrin, Nanocomposite, Photocatalyst  
D:

Padtaraporn Chanhom : METALLOPORPHYRIN-SENSITIZED  
TITANIA/SILICA/IRON OXIDE NANOCOMPOSITES AND THEIR  
PHOTOCATALYTIC ACTIVITIES. Advisor: Asst. Prof. Numpon Insin,  
Ph.D.

New nanomaterials of the magnetic visible light active photocatalysts, tetra(4-carboxyphenyl)porphyrin (TCPP) with different metals [Mn(II), Fe(III), Cu(II), Zn(II) and metal-free] in the center adsorbed on titania-silica-iron oxide superparamagnetic composites (TSI) were synthesized successfully. The photocatalytic activities in methylene blue (MB) degradation were determined under incandescent lamp for 3 h. Their characteristics have been identified using UV-visible spectroscopy, X-ray diffractometry (XRD), transmission electron microscopy (TEM), Fourier transform infrared spectroscopy (FT-IR), and X-ray photoelectron spectroscopy (XPS). The photodegradation results revealed that the metalloporphyrin sensitization helped TSI to absorb the light in visible region. Titania-silica-iron oxide nanomaterials with copper(II) tetra(4-carboxyphenyl)porphyrin (CuTCPP) can significantly eliminate methylene blue (MB) and *Escherichia coli* (*E. coli*) upon 3 h of irradiation. The four-cycled reuse without regeneration of the CuTCPP-TSI results supported the great reusability with the ease in magnetic separation due to high magnetic response of the nanocomposites. The photodegradation activity is not only dependent on the type of metal in metalloporphyrin, but many factors including content of the loaded porphyrin also influence the activity. The suitable condition for CuTCPP-TSI nanocomposite preparation is 0.01 mmol of CuTCPP per 50 mg of TSI using stirring at 60 °C for 12 h. Consequently, the visible light activated photocatalysts were favorably synthesized and able to apply in photooxidative reaction in various applications.

จุฬาลงกรณ์มหาวิทยาลัย  
CHULALONGKORN UNIVERSITY

Field of Study: Chemistry

Student's Signature

Academic Year: 2018

Advisor's Signature

Year:

.....

## ACKNOWLEDGEMENTS

First of all, I would like to express great gratitude to Assistant Professor Dr. Numpon Insin, my thesis advisor, who gave valuable suggestions, assistance and several encouragements throughout my work. His great kindness, attention and forbearance to my research and me are some of the important part for achievement of this thesis.

In addition, this research would not have been completed without all my thesis committee, Associate Professor Dr. Vudhichai Parasuk, Associate Professor Dr. Khanitha Pudhom, Dr. Wipark Anutrasakda, and Dr. Nisanart Charoenlap for their valuable advice and comments.

Furthermore, I would like to thank all members of Materials Chemistry and Catalysis Research Unit who always gave encouragement, laughter and useful help. Particularly, Miss Wishulada Injumba, Miss Jamornpan Yangcharoenyuenyong, Mr.Chonnavee Manipuntee, Dr.Chalathan Saengruengrit, who are my seniors that gave me very useful advises.

Other special group, I would to express my greatest gratitude to my family and good friends for their love, good wishes and encouragement at all times.

Finally, this work was partly funded by the Research Assistantship Funding from Faculty of Science, Chulalongkorn University. My graduate study was financially supported by the 100th Anniversary Chulalongkorn University Fund for Doctoral Scholarship, Graduate School and the 90th Anniversary of Chulalongkorn University Fund. Moreover, I would like to thank Department of Chemistry, Faculty of Science, Chulalongkorn University.

Padtaraporn Chanhom

# TABLE OF CONTENTS

	<b>Page</b>
.....	iii
ABSTRACT (THAI) .....	iii
.....	iv
ABSTRACT (ENGLISH) .....	iv
ACKNOWLEDGEMENTS .....	v
TABLE OF CONTENTS .....	vi
LIST OF FIGURES .....	viii
LIST OF TABLES .....	xii
LIST OF ABBREVIATIONS .....	xiii
CHAPTER I INTRODUCTION .....	1
1.1 Statement of the problem .....	1
1.2 Objectives of the thesis .....	2
1.3 Scope of the thesis .....	2
1.4 The benefits of this thesis .....	3
CHAPTER II THEORY AND LITERATURE REVIEW .....	4
2.1 Photocatalyst .....	4
2.2 Superparamagnetism .....	8
2.3 Porphyrins .....	12
2.4 Bacteria .....	12
2.5 Literature reviews .....	13
CHAPTER III EXPERIMENTS .....	22
3.1 The instruments and chemicals .....	22
3.2. Materials syntheses and characterization .....	23
3.2.1 Synthesis of porphyrin-sensitized titania nanocomposites .....	24

3.2.2 Synthesis of TSI nanocomposites with different metal centers to study the effect of metal in metalloporphyrin on the photocatalytic performance of the nanocomposites .....	26
3.2.3 Synthesis of TSI nanocomposites with different anchoring groups and the effect of the anchoring group on the photocatalytic performance.....	28
3.3 Characterization of the as-synthesized nanocomposites.....	30
3.4 Photocatalytic degradation measurement .....	32
3.4.1 The effect of metal centers in porphyrin on the photocatalytic degradation performance under visible irradiation .....	32
3.4.2 The effect of anchoring group between porphyrins and titania on the photocatalytic degradation performance under visible irradiation.....	32
3.4.3 Reusability of the nanocomposites.....	33
3.4.4 The effect of MB concentration on the photocatalytic degradation performance under visible irradiation .....	33
3.5 Antibacterial activity .....	33
CHAPTER IV RESULTS AND DISCUSSION .....	34
4.1 Characterization of metalloporphyrin-sensitized titania particles and their photodegradation results.....	34
4.1.1 Effects of metal center in porphyrin on the photocatalytic degradation performance under visible irradiation .....	36
4.2 Characterization of metalloporphyrin-sensitized TSI nanocomposites and their photodegradation results.....	39
4.2.1 Effects of metal center in porphyrin on the photocatalytic degradation performance under visible irradiation .....	39
4.2.2 The effect of the different anchoring group on the photocatalytic performance.....	57
4.2.3 Reusability of the nanocomposites.....	61
4.3 Antibacterial activity .....	64
CHAPTER V CONCLUSION.....	66
REFERENCES .....	68
VITA.....	72



## LIST OF FIGURES

	<b>Page</b>
Figure 2.1 Three phases of titania: anatase, rutile, and brookite .....	5
Figure 2.2 The processes of heterogeneous photocatalytic degradation of organic dye pollutants on titania nanoparticles under UV irradiation .....	6
Figure 2.3 Scheme for degradation pathway of MB under irradiation with titania photocatalysts .....	8
Figure 2.4 Schematic representation of multidomain (ferromagnetism) and single domain (superparamagnetism) .....	8
Figure 2.5 Schematic representation of superparamagnetic particles in presence and absence magnetic field .....	9
Figure 2.6 Schematic representation of different aggregates of surfactants between micells and reverse micelles .....	11
Figure 2.7 Illustration of microemulsion process for the silica coating on the iron oxide nanoparticles .....	11
Figure 2.8 SEM image of <i>E. coli</i> .....	13
Figure 2.9 Diagram of recombination between the photogenerated electron and hole	14
Figure 2.10 Band gap energy of the TSI nanocomposites .....	15
Figure 2.11 Proposed photoproduced of ROS mechanism for titania particles under visible irradiation .....	16
Figure 2.12 Photocatalytic degradation of methylene blue using CuTCPP-TiO <sub>2</sub> as catalyst coated on cotton .....	17
Figure 2.13 Representation of (a) TCPP-NH <sub>2</sub> -V-TiO <sub>2</sub> and (b) TCPP-V-TiO <sub>2</sub> structures .....	18
Figure 2.14 Representation of (a) FeTCPP-SA-TiO <sub>2</sub> and (b) FeTCPP-SSA-TiO <sub>2</sub> structures .....	19
Figure 2.15 Schematic illustration of the process of photo-killing of <i>E. coli</i> on TiO <sub>2</sub> film .....	20
Figure 3.1 Scheme for the synthesis of MTCPP-sensitized titania composites.....	24
Figure 3.2 Scheme for the synthesis of MTCPP-sensitized TSI nanocomposites .....	26
Figure 3.3 Scheme for the synthesis of MTCPP-TSI composites using the adsorption .....	28

Figure 3.4 Scheme for the synthesis of MTCPP-TSI composites using stirring at 60 °C .....	29
Figure 3.5 Scheme for the synthesis of MTCPP-TSI composites using the 2-hydroxy-5-sulfosalicylic acid (SSA) as a bridging molecule.....	29
Figure 3.6 Scheme for the synthesis of MTCPP-TSI composites using the covalent attachment.....	30
Figure 4.1 DR-UV spectra of TCPP-TiO <sub>2</sub> samples.....	34
Figure 4.2 The nitrogen adsorption-desorption isotherms of (a) 0.4 mM TCPP-TiO <sub>2</sub> , (b) 1 mM TCPP-TiO <sub>2</sub> , (c) 4 mM TCPP-TiO <sub>2</sub> .....	35
Figure 4.3 The DR-UV spectra of MTCPP-TiO <sub>2</sub> sample with the different metal centers or free-base compared to TiO <sub>2</sub> .....	36
Figure 4.4 XRD patterns of (a) TiO <sub>2</sub> , (b) TCPP-TiO <sub>2</sub> , (c) MnTCPP-TiO <sub>2</sub> , (d) FeTCPP-TiO <sub>2</sub> , (e) CuTCPP-TiO <sub>2</sub> , (f) ZnTCPP-TiO <sub>2</sub> , (g) JCPDS no. 21-1272 .....	37
Figure 4.5 The photodegradation of MB using various TCPP-TiO <sub>2</sub> samples and the bare TiO <sub>2</sub> .....	38
Figure 4.6 The photodegradation of MB using MTCPP-TiO <sub>2</sub> samples.....	39
Figure 4.7 The UV-vis spectra of CuTCPP-TSI samples .....	39
Figure 4.8 UV-Vis absorption spectra of (a) TSI, (b) TCPP and TCPP anchored on TSI, (c) MnTCPP and MnTCPP anchored on TSI, (d) FeTCPP and FeTCPP anchored on TSI, (e) CuTCPP and CuTCPP anchored on TSI, and (f) ZnTCPP and ZnTCPP anchored on TSI nanocomposites .....	40
Figure 4.9 FT-IR spectrum of CuTCPP.....	42
Figure 4.10 FT-IR spectra of (a) TSI composites, (b) TCPP-TSI composites, (c) MnTCPP-TSI composites, (d) FeTCPP-TSI composites, (e) CuTCPP-TSI composites, (f) ZnTCPP-TSI composites .....	43
Figure 4.11 X-ray diffraction patterns of (a) TSI composites, (b) TCPP-TSI composites, (c) MnTCPP-TSI composites, (d) FeTCPP-TSI composites, (e) CuTCPP-TSI composites, (f) ZnTCPP-TSI composites .....	44
Figure 4.12 The TEM images of (a) TSI nanocomposites and (b) CuTCPP-TSI nanocomposites.....	46
Figure 4.13 The selected area electron diffraction pattern of CuTCPP-TSI nanocomposites.....	47
Figure 4.14 SEM images of the CuTCPP-TSI and the EDX elemental mapping for Cu element .....	47

Figure 4.15 EDX spectra of CuTCPP-TSI composites.....	48
Figure 4.16 Hydrodynamic size distribution of TSI and CuTCPP-TSI dispersed in ethanol.....	49
Figure 4.17 High-resolution XPS spectra of (a) Mn 2p of MnTCPP and MnTCPP-TSI, (b) Fe 2p of FeTCPP and FeTCPP-TSI (c) Cu 2p of CuTCPP and CuTCPP-TSI, and (d) Zn 2p of ZnTCPP and ZnTCPP-TSI nanocomposites .....	51
Figure 4.18 Magnetization curves obtained at room temperature of the (a) iron oxide nanoparticles (I), and (b) CuTCPP-TSI nanocomposites .....	52
Figure 4.19 Photodegradation activity of methylene blue (MB) with 10 mg of each photocatalyst after 3h of irradiation.....	53
Figure 4.20 Photodegradation activity of methylene blue (MB) under 3h of irradiation with the same amount of porphyrin attached on TSI surface .....	54
Figure 4.21 Energy level diagram of different metalloporphyrins and free-metal porphyrin compared to conduction band of titania on TSI composites .....	55
Figure 4.22 At the different concentration of MB photodegradation upon 3 h of irradiation using CuTCPP-sensitized TSI nanocomposite (CuTCPP-TSI) .....	56
Figure 4.23 The UV-Vis spectra of CuTCPP-TSI samples with the different synthesized method (a) adsorption for 3 days, (b) stirring at 60 °C, (c) DCC coupling, (d) SSA as bridging molecule .....	57
Figure 4.24 XPS spectrum of S 2p in CuTCPP-TSI-SSA sample.....	58
Figure 4.25 FT-IR of CuTCPP-TSI samples with the different synthesized method (a) adsorption for 3 days, (b) stirring at 60 °C, (c) DCC coupling, (d) SSA as bridging molecule.....	58
Figure 4.26 Photodegradation activity of methylene blue (MB) under 3h of irradiation based on the same amount of catalysts with different anchoring groups .....	59
Figure 4.27 Photodegradation activity of methylene blue (MB) under 3h of irradiation based on the same amount of porphyrin attached on CuTCPP-TSI surface with the different anchoring group .....	60
Figure 4.28 The photodegradation of methylene blue upon visible light irradiation using CuTCPP-sensitized TSI nanocomposite (CuTCPP-TSI) in different cycles of reused CuTCPP-TSI.....	61
Figure 4.29 (a) The standard calibration curve of copper ion and (b) The concentration of copper ion in the MB solution after photodegradation reaction.....	62

Figure 4.30 Diffuse reflectance UV-vis absorption spectra of CuTCPP-TSI before the photooxidation reaction of MB solution and after the fourth cycle of reuse. ....63

Figure 4.31 The bactericidal activity with non-activated and visible-light-activated CuTCPP-TSI nanocomposites at 0 mg/L (black bar), 17.5 mg/L (light gray bar) and 20.0 mg/L (dark gray bar) within 3 h of irradiation. ....64

Figure 4.32 The antibacterial activity of CuTCPP-TSI against *E. coli*. ....65



## LIST OF TABLES

	<b>Page</b>
Table 3.1 List of the instruments .....	22
Table 3.2 List of the chemicals .....	23
Table 3.3 The abbreviated name for each metalloporphyrins.....	25
Table 3.4 Temperature controlled program for the syntheses of monodisperse iron oxide nanoparticles .....	27
Table 4.1 Specific surface area values of TCPP-TiO <sub>2</sub> samples .....	36
Table 4.2 The estimated crystalline sizes of magnetite calculated using the Debye-Scherrer equation .....	45
Table 4.3 The calculated d-spacings of CuTCPP-TSI measured using TEM-SAED technique.....	47
Table 4.4 The elements in CuTCPP-TSI composites .....	48
Table 4.5 The average particle sizes of TSI and CuTCPP-TSI determined using a dynamic light scattering (DLS) analysis.....	49
Table 4.6 The percentage of nitrogen in TSI and TSI-NH <sub>2</sub> from CHSN elemental analysis.....	57



## LIST OF ABBREVIATIONS

I	=	Iron oxide nanoparticles
SI	=	Silica-coated iron oxide nanoparticles
TSI	=	Titania-silica-iron oxide nanocomposites
TCPP	=	Tetra(4-carboxyphenyl)porphyrin
SSA	=	2-Hydroxy-5-sulfosalicylic acid
FT-IR	=	Fourier transform infrared spectrometer
TEM	=	Transmission electron microscope
XRD	=	X-ray diffractometer
XPS	=	X-ray photoelectron spectrometer
SEM	=	Scanning electron microscope
ICP-OES	=	Inductively coupled plasma-optical emission spectrometer
DLS	=	Dynamic light scattering spectrometer
EDX	=	Energy dispersive X-ray spectrometer
UV	=	Ultra violet
G	=	Gram
Mg	=	Milligram
L	=	Liter
mL	=	Milliliter
Ppb	=	Parts per billion

# CHAPTER I

## INTRODUCTION

### 1.1 Statement of the problem

Titania (titanium dioxide) is a very well-known and well-used photocatalyst because of its various properties such as low toxicity, low cost, high chemical stability and especially good photocatalytic activity upon ultraviolet (UV) region [1, 2]. Nevertheless, there are limitations such as the use of titania slurry because it is difficult to separate and recover these small particles from the liquid media. In order to solve the separation problem, some researchers made materials that are composed of magnetic nanoparticle cores and titania shells [3]. In our previous study [4], our results showed that the titania-coated magnetic nanoparticles (TI) provided lower photoredox activity than the titania itself due to the increasing recombination rate of electron and hole. Iron oxide core inside this composite can be served as the recombination center of photogenerated electrons and holes. After the synthesis of TSI nanocomposites and investigation of their photocatalytic activity, we found that the amorphous silica could prevent the direct electrical contact between the magnetic core and the titania shell.

TSI nanocomposites not only have high photocatalytic performance under UV irradiation but also these composites can be readily recovered by applying an external magnetic field. However, TSI nanocomposites have some limitation in practical applications such as their effective photo-response to only UV irradiation, which accounts for only 4-6% of the solar spectrum [5]. Hence, the use of metalloporphyrin as light harvesters on titania is particularly attractive. Metalloporphyrin is an appropriate sensitizer because of its high absorption coefficient within the solar spectrum and its high stable for the chemical reactions in comparison to other dyes. In this work, tetra(4-carboxyphenyl)porphyrin complexes (TCPP) with various metal centers were used as sensitizers and conjugated onto titania surface of TSI nanoparticles. The combination of the two materials leads to multifunctionality, and

the synergy of magnetic and photocatalytic properties under visible light suitable for many applications that require magnetic separation and magnetic guide such as organic dye degradation and the eradication of pathogenic bacteria.

## **1.2 Objectives of the thesis**

1.2.1 To prepare novel nanocomposites of TSI with metalloporphyrin attached on the surface

1.2.2 To characterize the physical properties of the composites using XRD, XPS, TEM and UV-visible spectroscopy

1.2.3 To investigate the photocatalytic efficiency of the nanocomposites in methylene blue degradation and bactericidal activity under visible light

## **1.3 Scope of the thesis**

The scope of this research starts with the synthesis of the titania-silica-iron oxide nanocomposites with metalloporphyrin as a sensitizer attached to the titania shell. The methods for composite preparation were designed by aiming at obtaining the magnetic composites with high photocatalytic activity under visible light and superparamagnetic behavior. The obtained nanocomposites will then be characterized using X-ray diffraction (XRD), transmission electron microscope (TEM), X-ray photoelectron spectrometer (XPS), and UV-visible spectrophotometer. After obtaining the nanocomposites, these nanocomposites were used as photocatalysts for MB degradation upon visible irradiation. Then, their separations were investigated after used. For the ease of separation, reusability of the composites for the degradation of methylene blue (MB) solution under visible irradiation will be studied. The study also aims at measuring the bactericidal activity of the synthesized nanocomposites.



#### **1.4 The benefits of this thesis**

1.4.1 The new visible light activated photocatalysts with magnetic response were produced to apply in water treatment.

1.4.2 The effect of metal centers in metalloporphyrins on the photodegradation performance and the effect of anchoring group between porphyrin and titania has been investigated.

1.4.3 The prepared photocatalysts could be utilized in antibacterial application



## CHAPTER II

### THEORY AND LITERATURE REVIEW

#### 2.1 Photocatalyst

Photocatalyst is a material that is sensitively responsive to redox reaction upon the activation by UV radiation and then free radicals were easily produced. Many photocatalysts such as titanium dioxide ( $\text{TiO}_2$ ) or zinc oxide ( $\text{ZnO}$ ) have been widely used as a catalyst under UV activation for degradation of pollutant organic molecules, self-cleaning surface, water splitting, oxidation of organic molecules and eradication of pathogenic bacteria [1, 6]. Among many photocatalysts, titania nanoparticles have been attempted as the highest performance catalyst because of its great catalytic efficacy, non-toxicity, chemical stability and low cost [1, 2]. Photodegradation process is a new system that has been used to degrade pollutants that might contain in environment. Finally, after degradation with photocatalyst, the products with less hazardous species such as water molecules, carbon dioxide gas and inorganic ions are obtained.

Titanium dioxide or titania ( $\text{TiO}_2$ ) exists as three different crystal structures, which are anatase, rutile and brookite. The different crystal structures of titania are shown in Figure 2.1. Through at the crystal structures titanium is coordinated octahedrally to six oxygen ( $\text{O}^{2-}$ ) atoms at equal distances, forming  $\text{TiO}_6$ . For anatase case, four edges of octahedral  $\text{TiO}_6$  are shared. While two edges of  $\text{TiO}_6$  are shared in case of rutile. Brookite is made up of the distorted  $\text{TiO}_6$  octahedral sharing three edges. Both of anatase and rutile forms are of the tetragonal crystal structures. Brookite has a conformation belonging to the orthorhombic crystal structure. The overall stoichiometry is  $\text{TiO}_2$ . Anatase and rutile are usually formed depending on the synthesis condition, while brookite is rather unstable and not obtainable normally. Anatase titania phase is commonly considered as the best phase for catalyst application under UV irradiation as it gives a higher photocatalytic property than the

other types of titania because it has a higher reduction potential and give a slower recombination rate between electron-hole pairs [2].

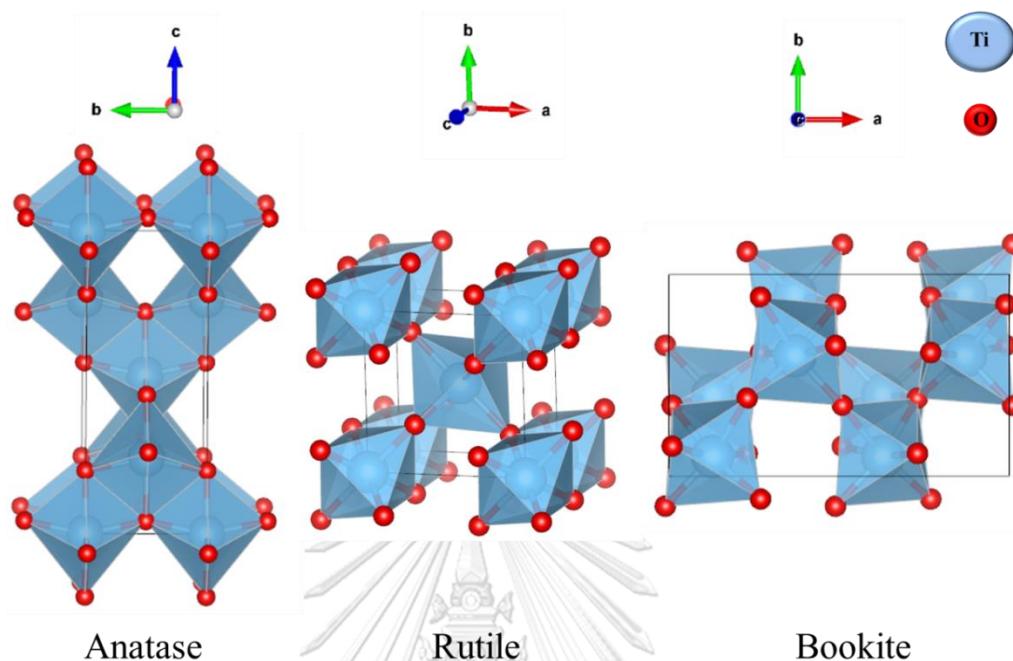


Figure 2.1 Three phases of titania: anatase, rutile, and brookite [1]

### Mechanism of photocatalytic degradation of organic dye pollutants

The photodegradation principles of organic pollutants can be easily concluded as follows [1, 2]. The titania is a semiconductor characterized by its electronic band structure according to the band theory of solid. The higher occupied energy band and the lowest empty energy band are called valence band and conduction band, respectively. A distance between them is called band gap. When an electron on the valence band (VB) is activated under irradiation by a photon with energy equals to or exceeds the band gap of the photocatalyst, electron ( $e^-$ ) can be promoted from the valence band to the conduction band. Consequently, an electron vacancy, a photogenerated hole ( $h^+$ ) exists in the valence band. The photogenerated electron on the conduction band, which works as a reducing reagent, can be donated to an electron acceptor such as an molecular oxygen. Reactive radicals or reactive oxygen species (ROS) e.g. superoxide radicals and hydroxyl radicals formed could oxidize organic substances. Simultaneously, the photogenerated hole acts as an oxidizing reagent, potentially oxidize water molecules to hydroxyl radicals. The photocatalytic redox reaction of organic dyes and pollutants is illustrated in Figure 2.2.

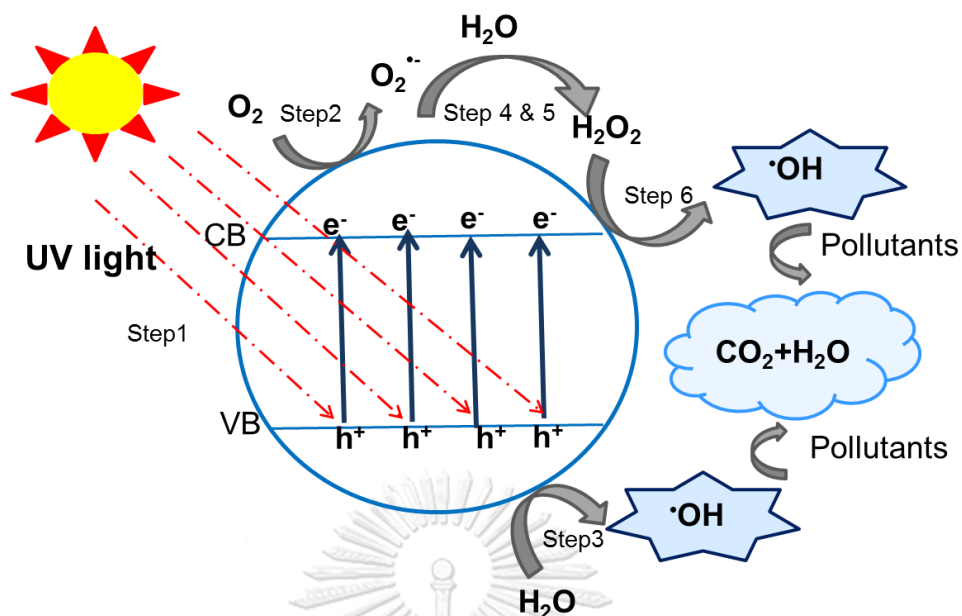
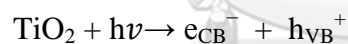


Figure 2.2 The processes of heterogeneous photocatalytic degradation of organic dye pollutants on titania nanoparticles under UV irradiation [1]

The causes of the photoredox reaction of organic pollutants were described in deep detail, according to all following equations [1, 2].

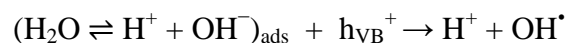
1. Excitation of the titania by photons ( $h\nu \geq E_g = 3.2 \text{ eV}$ )



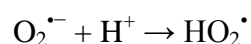
2. Oxygen ionosorption (first reduction of oxygen)



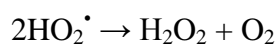
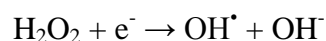
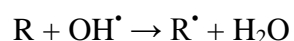
3. Neutralization of OH<sup>-</sup> by photogenerated holes that produces OH•



4. Neutralization of O<sub>2</sub><sup>•-</sup> by protons



## 5. Transient hydrogen peroxide formation

6. Decomposition of  $\text{H}_2\text{O}_2$  (second reduction of oxygen)7. Oxidation of the organic reactant (R) via continuous attacks by  $\text{OH}^\bullet$  radicals

It was reported that more than 15% of dyes production is lost and released from the produced dyes in textile industry [7]. Dye compounds are an important source of non-aesthetic pollution and eutrophication in ecosystems. Methylene blue (MB) ( $\text{C}_{16}\text{H}_{18}\text{ClN}_3\text{S}$ ), a cationic thiazine dye, is regularly chosen to be the model dye for study about photodegradation. When it is still in solid form, it appears as dark green powder. When it is dissolved in water, it becomes a brightly blue solution. In previous studies, some researchers proposed the pathway of MB photodegradation under UV irradiation as shown in Figure 2.3 [7]. During the photocatalytic degradation, the generated intermediates were identified using GC/MS and LC/MS.

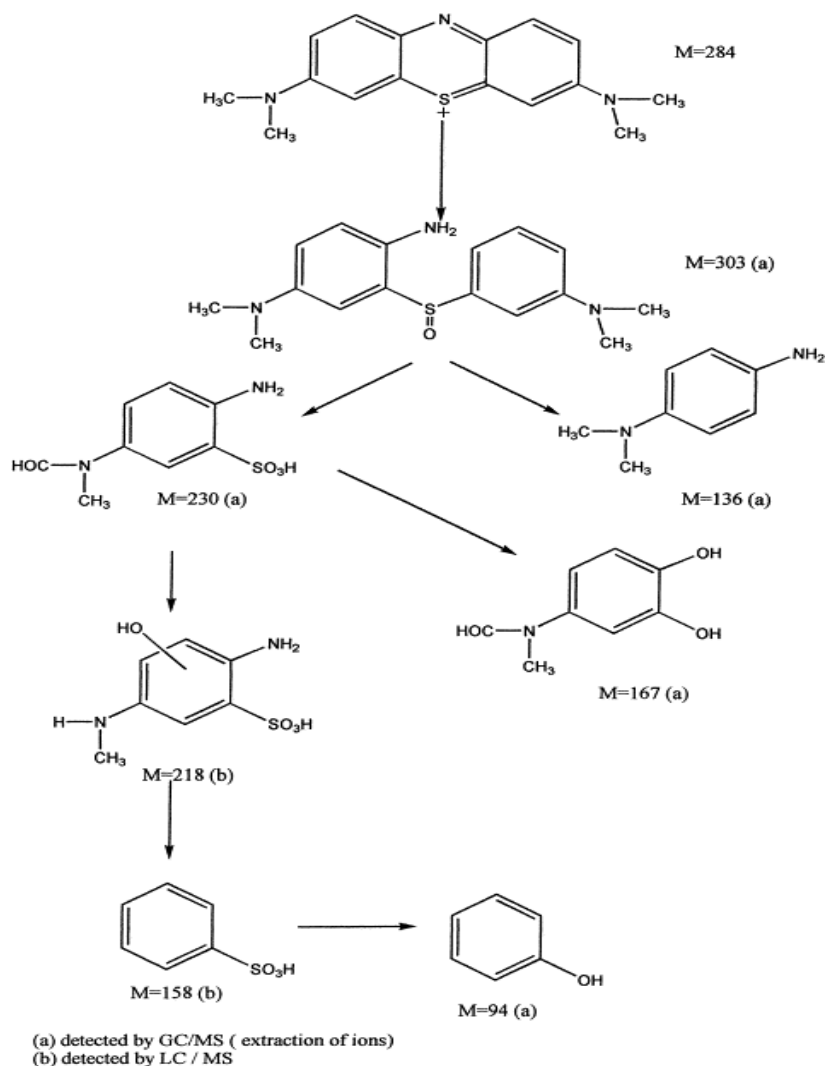


Figure 2.3 Scheme for degradation pathway of MB under irradiation with titania photocatalysts [7]

## 2.2 Superparamagnetism

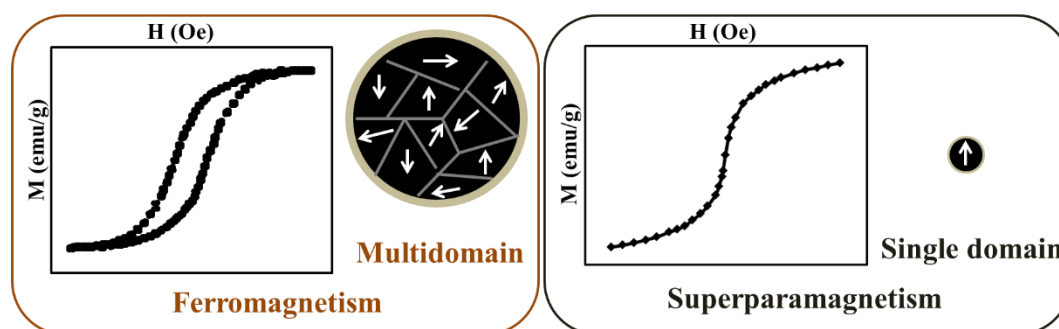
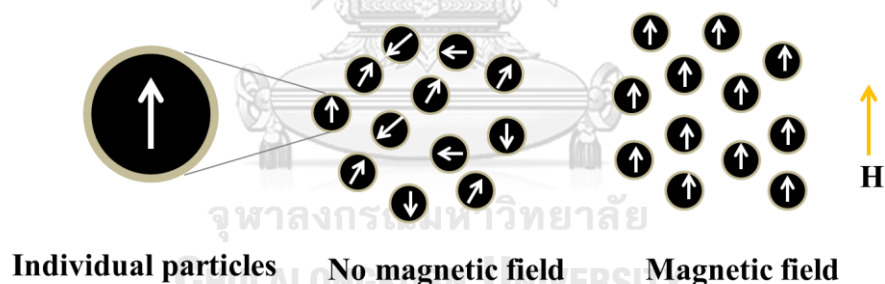


Figure 2.4 Schematic representation of multidomain (ferromagnetism) and single domain (superparamagnetism) (white arrow shows the net magnetic moment each particles) [8].

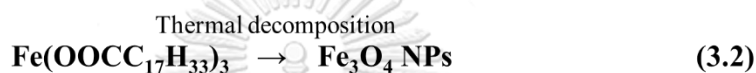
Superparamagnetism phenomenon appears in small size of ferromagnetic nanoparticles, which are single domain state. Ferromagnetic particles are the materials which come from the arrangement of coupled unpaired electrons. The materials exhibit permanent magnetism and strong magnetic responses when they were under magnetic field. Magnetic nanoparticles display different properties from bulk materials. The important behavior of superparamagnetism is no magnetic attractions in the absence of a magnetic field. There is no residual magnetization, remnant magnetization, resulting in disappearance of hysteresis loop as shown the magnetic curve compared to ferromagnetic materials in Figure 2.4. However, if you apply an induction of magnetic field, magnetic moment of these materials can be arranged in the same direction of magnetic field (Figure 2.5). Hence, when no external field is present, it shows colloidal stability and dispersibility in solution. Superparamagnetism displays the changing of behavior between the characters of ferromagnetism under an induction of magnetic field and the paramagnetism when the materials were in absence of the magnetic field as the random magnetic moment in single nanoparticles can be easily rearranged under the presence of magnetic field [8].



*Figure 2.5 Schematic representation of superparamagnetic particles in presence and absence magnetic field (white arrow shows the net magnetic moment each particles) [8].*

Superparamagnetic materials are commonly utilized in many applications because these small particles have high specific surface area, colloidal stability, the large amount of atom for serving as the center of reaction at the surface and ease in the separation by applying a magnetic field [8]. There are various methods available to synthesize iron oxide nanoparticles such as microemulsion, co-precipitation, sol-gel, hydrothermal and thermal decomposition [9]. All of them are able to prepare high-quality magnetic particles. However, thermal decomposition is a method that has been improved and investigated the factors for the sizes and shapes control to form

monodisperse nanoparticles. The nanoparticles were synthesized through the thermal decomposition of desired precursors and surfactants. In presence of stabilizing surfactants, precursors were decomposed in high temperature organic solvents, leading to the presence of monodisperse with superparamagnetic behavior. The ratios of the starting reagents, the reaction time and reaction temperature were control to obtain the desired size and morphology of magnetic nanoparticles. Monodispersed superparamagnetic iron oxide materials were synthesized using a two-step process following to reaction Equations 3.1 and 3.2 [10].



For silica and titania coating on the superparamagnetic materials, the reverse microemulsion method was selected due to the ease in obtaining the core-shell structure. Microemulsion-based synthesis is a versatile route to prepare nanomaterials with varied size and shape. The word “microemulsion or micelles” is two immiscible liquids that can be formed stable dispersion [11]. It is mainly aggregation of surfactant-surrounded hydrophobic solvent dispersed in aqueous solution. For reverse microemulsion, it is formed surfactant aggregation in nonaqueous media. The hydrophilic groups (polar head group) point toward the center of this micelle as the same time the hydrophobic groups (long alkyl chain) of surfactants point toward to the nonaqueous media. The important parameters for preparing nanoparticle size and distribution are controlled using the ratios between aqueous and nonaqueous solution, reaction rate, temperature, time, the content of catalyst and precursor [12-14]. The final products are precipitated by the addition of solvent (ethanol or acetone) into reaction solution after the reaction was completed (Figure 2.6).



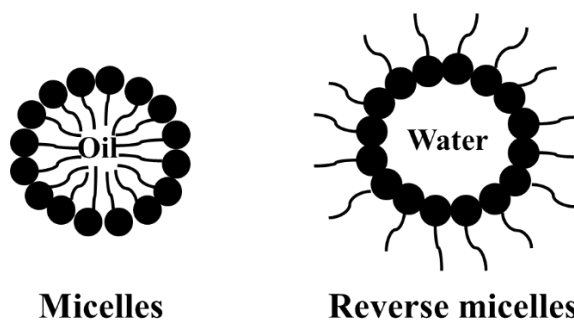


Figure 2.6 Schematic representation of different aggregates of surfactants between micells and reverse micelles

The silica coating process on the iron oxide nanoparticles via the reverse microemulsion method was proposed in Figure 2.7. Firstly, micelles were formed using dispersion of Igepal CO-520. The ligand exchange reaction occurred after adding iron oxide nanoparticles. The oleates on the surface of superparamagnetic particles are replaced by Igepal CO-520 surfactant. In the next step, reverse microemulsion system is formed after adding ammonia solution because the Igepal CO-520 surfactants are filled with ammonia solution, and the size of micelle is enlarged. Tetraethyl orthosilicate (TEOS) is added and hydrolyzed at the interface while the ligand exchange reaction with Igepal CO-520 chemically absorbed on the surface of superparamagnetic particles. After that, these particles are transferred to the other phase. Finally, the added TEOS is hydrolyzed on the surface, and the silica was completely coated [13].

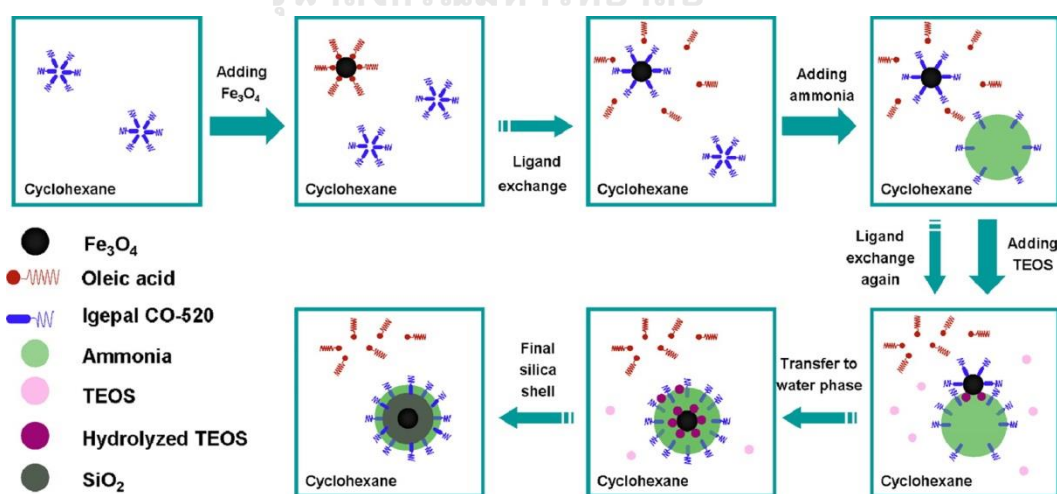


Figure 2.7 Illustration of microemulsion process for the silica coating on the iron oxide nanoparticles [13]

### 2.3 Porphyrins

Porphyrins are aromatic macrocyclic compounds consisting of four pyrrole rings linked together *via* methine (=CH-) bridges to give a highly conjugated macrocycle.

Generally, porphyrin molecule is cyclic eighteen conjugated  $\pi$ -electrons system forming macrocyclic compounds. Porphyrins show high thermal and chemical stability because they have electrons which can delocalize in their molecules. Moreover, porphyrins show strong absorption in the visible region. Porphyrins exhibit an intense Soret band in the absorption spectrum with high extinction coefficients at around 400 nm. Porphyrins have other bands between 450 to 700 nm, which are called Q bands [15, 16].

A free-base porphyrin containing metal inserted in its cavity or at the center is called metalloporphyrin. Some metalloporphyrins commonly play important role in biological redox reactions. The intensity and wavelength in porphyrins are changed due to insertion of metal into the porphyrin cavity [16].

### 2.4 Bacteria

Bacteria are prokaryotic cell. They have both DNA and RNA, but they do not possess nuclear membrane nor nucleus in cell. Thus, they can exhibit all fundamental life process such as metabolism, growth and reproduction. We can find them everywhere on the earth for example in the air, soil, water etc. They are mainly divided into three types of shape: coccus (sphere), bacillus (rod), and spiral. Generally, they have diameter falling in the range of 0.3 to 2 micrometers. They are often maligned as the causes of human and animal disease.

*Escherichia coli* (*E. coli*)

*E. coli* is a Gram-negative rod bacterium that can be considered as an average sized bacterium with average cell length in the range of 1 to 2 micrometers (Figure 2.8). They are facultative anaerobe. They are member in *Enterobacteriaceae* family and belong to coliform group which contains motile peritrichous flagella. Normally, *E. coli* cells are consumed in contaminated food or are transmitted through insect, they can cause the diseases in gastrointestinal tract. They can be found in intestinal

tract of human and animal. The result from infection of *E. coli* can be found in three clinical diseases: diarrhea, urinary tract infections and meningitis in infants [17].

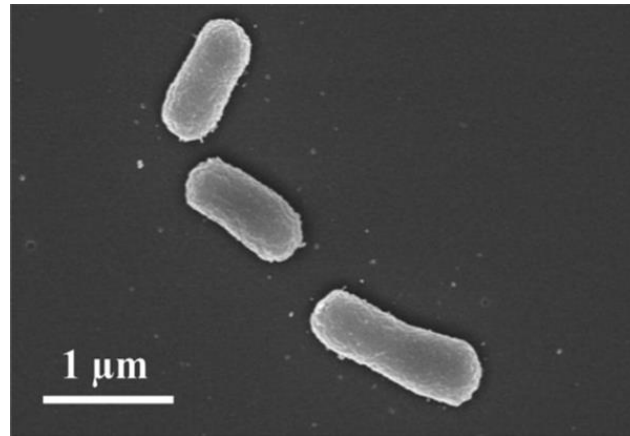


*Figure 2.8 SEM image of E. coli*

## 2.5 Literature reviews

Photocatalysis process has demonstrated to be an effective redox reaction for wastewater treatment. Titania has been fervently researched to be the most suitable candidate because of its potential properties across various different fields. Whenever the titania slurry is dispersed in aqueous medium, it requires a way for separation and further reuse. Nanocomposites with a magnetically responsive core and a titania shell are the combination of the magnetic responsive property with photocatalytic property that are useful in many applications such as environmental application. This is an economical and eco-friendly technology for future use. Several researchers worked on the synthesized titania-coated iron oxide nanocomposites (TI) [3, 18] revealed that these composites present a lower photodegradation property compared to titania itself because of the contraction of the magnetic core and photoactive shell leading to the recombination of electrons and holes at magnetic core under irradiation [3].

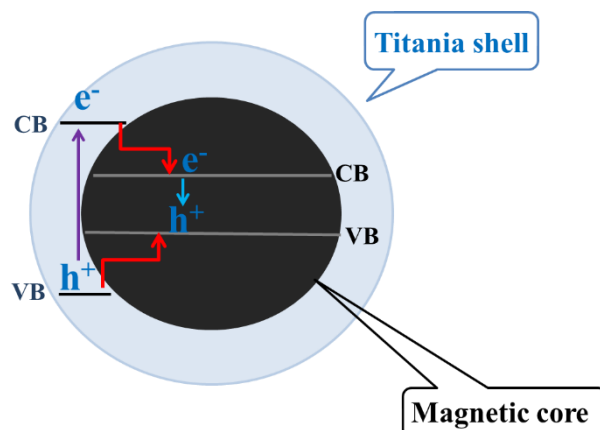


Figure 2.9 Diagram of recombination between the photogenerated electron and hole

From previous reports, energy level diagram of these composites (magnetite core and anatase titania shell) can be exhibited as in Figure 2.9. It is thermodynamically feasible for the photogenerated electrons located at the conduction band (CB) of titania to transfer to the magnetic core conduction band. Simultaneously the photogenerated holes from the titania valence band are transferred to the upper magnetic core valence band. Because the magnetic conduction band is of lower energy than the titania conduction band, hence the favorable electron transfer to magnetic core. Similarly, the valence band position of titania is lower than the magnetic core valence band; therefore, the electron at the magnetic core valence band can be moved to the titania valence band. This electron transfer could be viewed as the photogenerated hole transferring to the valence band of titania. Moreover, the magnetite band gaps (0.1 eV) are smaller than the titania band gap (3.20 eV). Based upon both the position and band gap energy, it is supportive that the electron-hole recombination at the magnetic core occurs. However, due to improper reduction potentials, unlike titania, the generated electrons cannot be captured by  $O_2$  molecules to form reactive oxygen species such as  $O_2^{\cdot-}$  radicals, while the generated holes are unable to oxidize water to hydroxyl radicals to perform photocatalytic reactions [18].

To overcome the limitations of the low photoactivities of titania-magnetite in direct contact, in our previous study we prepared three components model of titania/silica/iron oxide nanocomposites (TSI) [4]. In these TSI, a magnetic core acts as the magnetic separating agent for reuse. The large band gap energy of the silica interlayer between the magnetic core and titania shell can prevent the injection of

charges, and outer shells of a titanium dioxide perform photocatalytic activity. The results from comparing photodegradation of MB under UV irradiation between the titania-coated magnetic nanoparticles (TI) and the three component TSI magnetic photocatalysts indicated that the silica interlayer demonstrates significantly higher in photocatalytic property as the electron-hole recombination in magnetic nanoparticles is reduced. A wide bandgap silica can effectively improve the photocatalytic activities because the insulating silica could prevent the electron transfer between the two materials (titania shell and magnetic core), resulting in the decrease in the recombination between the electron and hole. Consequently, more reactive oxygen species such as superoxide radicals, hydroxyl radicals are generated on the TSI nanocomposite surface comparing with TI nanocomposites under UV irradiation for degradation of methylene blue. Furthermore, we observed that the silica layer thickness of at least 6 nm is enough for preventing the interaction between magnetic cores and titania shells leading to the TSI nanocomposites with high photocatalytic activities [4].

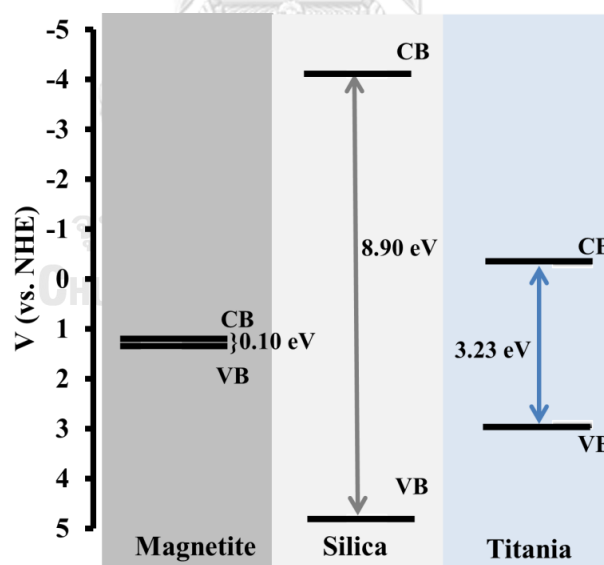


Figure 2.10 Band gap energy of the TSI nanocomposites [4]

Titania nanoparticles require UV irradiation in order to be a photoactive materials according to several previous reports[5]. The sunlight is mostly in visible region. Therefore, there is motivation to improve an efficient photocatalyst in the visible light-broaden to extend its spectral response to lower energy. Titania

nanoparticles can be improved by various methods [5] such as organic dyes sensitization, nonmetal doping, and metal doping. The sensitization method can effectively extend the range of visible light absorption. Moreover, porphyrin can be easily tuned its redox properties by metal complexation and has high chemical resistance when compared to other dyes [16]. Metalloporphyrins are regarded as efficient sensitizers to harvest light on the titania surface. Because of a substantial system of delocalized  $\pi$  electrons, porphyrins have very intense absorption in the visible light. The sensitization of titania nanoparticles by porphyrins is also regarded as an effective approach to enhance visible spectral absorption and photooxidative process of organic pollutants degradation such as methylene blue [19, 20] and  $\alpha$ -terpinene [21] under visible irradiation as reported previously. For the proposed mechanism (Figure 2.11) [21], the porphyrin adsorbed on the surface of titania can be excited by visible light, and photosensitization occurs by electron transfer from the excited porphyrin molecule to the conduction band of titania. Afterward, the reactive electrons in the conduction band can reduce  $O_2$  adsorbed on the surface of titania to superoxide radicals, which may be transformed into hydroxyl radicals. Moreover, water molecules as electron donors can reduce the oxidized porphyrin to porphyrin.

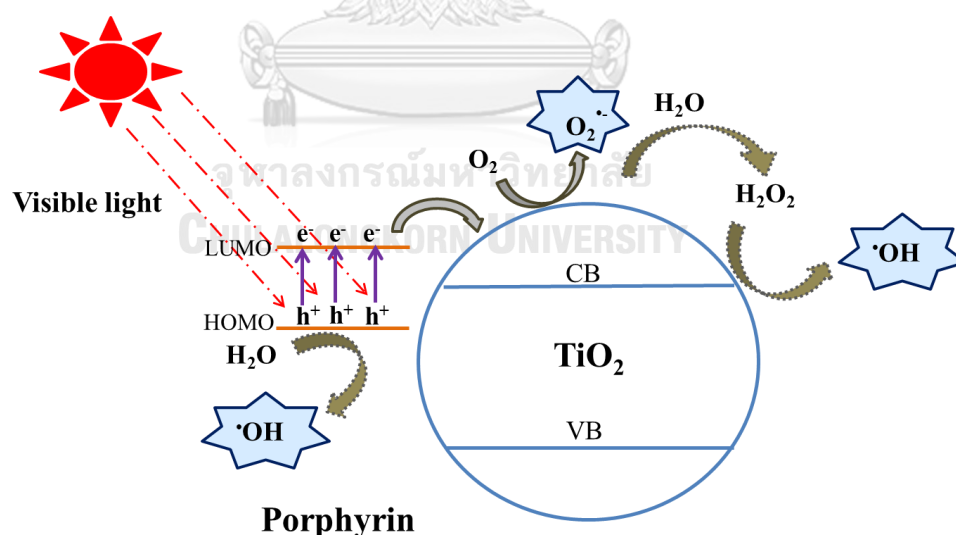


Figure 2.11 Proposed photoproduction of ROS mechanism for titania particles under visible irradiation [21]

Dye photosensitization has been one of the most effective ways to extend the photo-response of titania into the visible region. Examples of successful sensitization

TiO<sub>2</sub> with metalloporphyrins have been reported. Some researchers were interested in the thin films of tetra(4-carboxyphenyl)porphyrin (TCPP) or copper(II) tetra(4-carboxyphenyl)porphyrin (CuTCPP) with titania on the cotton fabrics [21]. They found that thin films of CuTCPP/TiO<sub>2</sub>-coated on cotton fabrics exhibited superior self-cleaning properties as compared to bare TiO<sub>2</sub>-coated cotton fabrics (Figure. 2.12). Moreover, thin films of CuTCPP/TiO<sub>2</sub>-coated on fabrics were highly photostable under visible-light when compared to TCPP/TiO<sub>2</sub>-coated cotton.

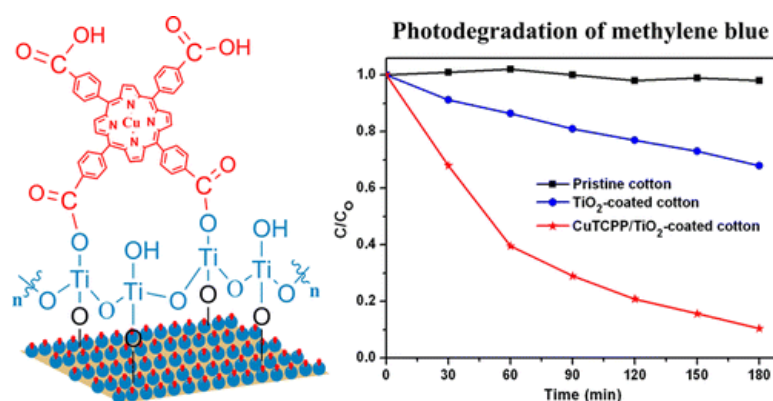


Figure 2.12 Photocatalytic degradation of methylene blue using CuTCPP-TiO<sub>2</sub> as catalyst coated on cotton [21]

For the effects of metals, the photocatalytic activity of TCPP with various metal centers (metal-free, Cu(II), Zn(II), Fe(III)) adsorbed on titania surface has been investigated by carrying out the degradation of atrazine under visible light [22]. Upon the addition of an optimized concentration of hydrogen peroxide, the maximum photocatalytic activity was achieved using meso-tetra(4-carboxyphenyl)porphyrinato copper(II) (CuTCPP) as photosensitizer (82% of degradation). The researchers observed that the metal porphyrin with unpaired electrons in d orbital such as Cu(II), Fe(III) showed higher photodegradation than Zn(II)-porphyrin and free-base porphyrin because Cu(II)-porphyrin and Fe(III)-porphyrin can reversibly coordinate with hydrogen peroxide, leading to an increase in production of hydroxyl radicals.

For the effects of metals, the photocatalytic activity of TCPP with various metal centers (metal-free, Cu(II), Zn(II), Fe(III)) adsorbed on titania surface has been investigated by carrying out the degradation of atrazine under visible light [22]. Upon the addition of an optimized concentration of hydrogen peroxide, the maximum

photocatalytic activity was achieved using meso-tetra(4-carboxyphenyl)porphyrinato copper(II) (CuTCPP) as photosensitizer (82% of degradation with adding 0.05 M  $\text{H}_2\text{O}_2$ ). The researchers observed that the metal porphyrin with unpaired electrons in d orbital such as Cu(II), Fe(III) showed higher photodegradation than Zn(II)-porphyrin and free-base porphyrin.

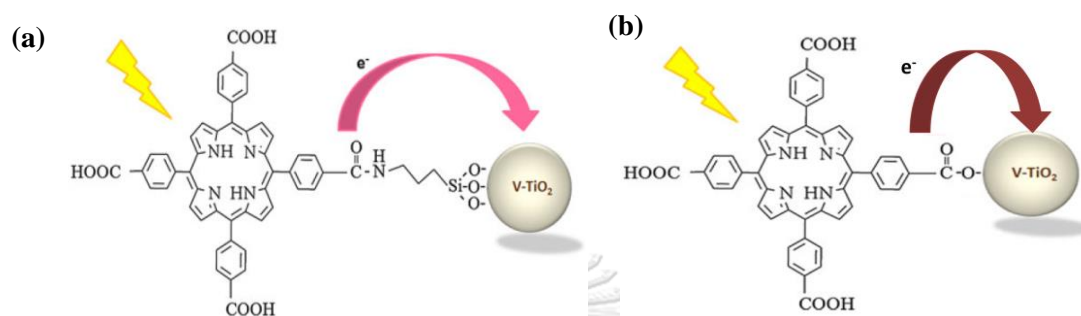


Figure 2.13 Representation of (a)  $\text{TCPP-NH}_2\text{-V-TiO}_2$  and (b)  $\text{TCPP-V-TiO}_2$  structures [23]

For the investigation of the effect of anchoring group of porphyrins and titania, two catalysts with different couplings between TCPP and vanadium doped titania ( $\text{V-TiO}_2$ ) surface, which are ester-like linkage ( $\text{TCPP-V-TiO}_2$ ) and amide-like linkage ( $\text{TCPP-NH}_2\text{-V-TiO}_2$ ) (Figure 2.13), were compared in the photodegradation of methyl orange (MO) solution [23]. It was found that  $\text{TCPP-V-TiO}_2$  exhibited higher photocatalytic activity than  $\text{TCPP-NH}_2\text{-V-TiO}_2$  and  $\text{V-TiO}_2$  under visible irradiation. The researchers reported that the ester bond acts as the better electron transfer channel between porphyrin and titania, and can improve the adsorption quantity of TCPP. Moreover, Yao *et al.* studied different conjugation of FeTCPP onto  $\text{TiO}_2$  by chemically linking the titania with FeTCPP as a sensitizer and the 2-hydroxy-5-sulfosalicylic acid (SSA) or salicylic acid (SA) as bridging molecule (Figure 2.14) [19]. The results showed that  $\text{FeTCPP-SSA-TiO}_2$  exhibited the best photocatalytic activity (99% of methylene blue degradation) under visible irradiation. They revealed that SSA plays as a bridging molecule that induced firm immobilization of metalloporphyrin on the surface of titania particles.



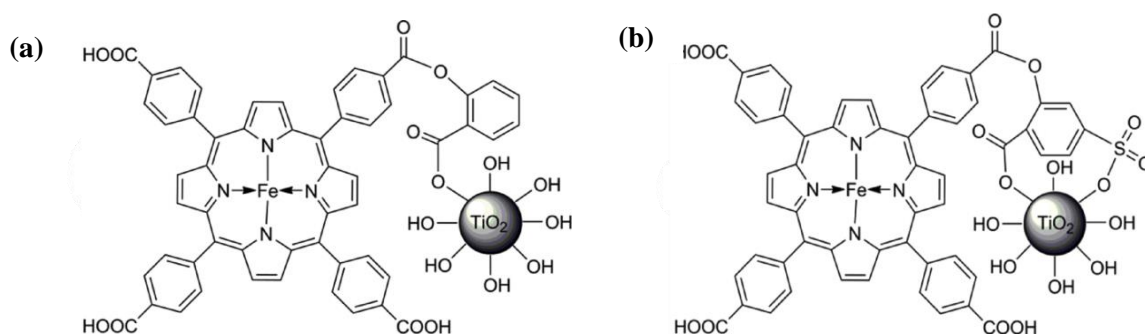


Figure 2.14 Representation of (a)  $FeTCPP-SA-TiO_2$  and (b)  $FeTCPP-SSA-TiO_2$  structures [19]

Besides, photocatalysis is an effective technology for elimination of pathogenic bacteria in water environment. Titania particles have been considered as effective alternatives to deactivate a variety of harmful bacteria. When titania photocatalysts are illuminated with UV irradiation,  $TiO_2$  accomplishes strong oxidizing power and can generate reductive oxygen species (ROS) such as  $OH^\bullet$  and  $O_2^{\bullet-}$ . Some researchers have confirmed that these ROS could destroy the outer membrane of the *Escherichia coli* (*E. coli*) cell, and finally the cells death occurs. Sunada *et al.* proposed the mechanism for photo-killing process of *E. coli* using titania as a catalyst as followed [24]. Figure 2.15a shows that the cell envelop of *E. coli*. consists of the following three layers (starting from the outside and moving inward): an outer membrane, a monolayer of peptidoglycan, and a cytoplasmic membrane. In the first step, the outer membrane is decomposed by the reactive species (ROS) produced by photocatalyst. The second step is the disordering of the cytoplasmic membrane. Then the cytoplasmic membrane is attacked by ROS, leading to the peroxidation of membrane lipid. Lipid peroxidation leads to the loss of cell viability (Figures 2.15 b-c).

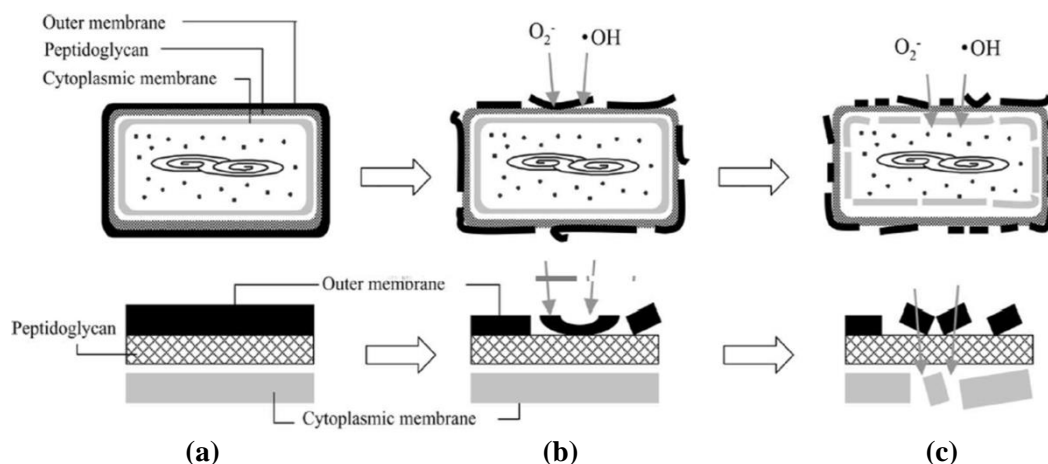


Figure 2.15 Schematic illustration of the process of photo-killing of *E. coli* on  $\text{TiO}_2$  film [24]

Recently, there have been many articles published about advances in bacterial disinfection. Visible light activated-titania photocatalytic materials are also reviewed here. A copper-doped  $\text{TiO}_2$  was produced for the killing activity of *E. coli* upon visible light irradiation [25]. The highest antibacterial activity of *E. coli* was reported in a moderate humidity. In addition, Zargari and co-workers synthesized graphene-titania nanocomposite with SnTCPP as sensitizer and demonstrated that the efficiency of photocatalytic inactivation of *E. coli* was 99.99% with the visible light irradiation [26]. However, the separation of materials after used in the disinfection is difficult. The as-synthesized magnetic photocatalyst would solve that problem because the superparamagnetic materials can be well dispersed in colloidal solution, when no external field is present, and could be more accessible to targets bacterial cells. These materials can be recovered easily when an external magnetic field is applied.

In this work, the visible light photocatalysts included superparamagnetic character were prepared using attachment of the porphyrin complex (TCPP) with various metal centers onto TSI composites. The main objective of this work is to evaluate the potential application of this kind of materials in water treatment and anti-bacteria under visible light. Measuring the degradation of MB solution upon visible light irradiation was demonstrated to compare the photocatalytic activities of the products to bare TSI nanocomposites. We investigated the different metals of TCPP on the photocatalytic performance, and the suitable conditions for the degradation of MB under visible light were studied. Furthermore, antibacterial activity against *E. coli*

of these nanocomposites upon visible irradiation was tested to reveal the visible light disinfection applications using the easily magnetically removable composites.



## CHAPTER III

### EXPERIMENTS

In this work, magnetic nanocomposites were synthesized and used as a photocatalyst for the MB degradation. The experiment chapter is divided into five sections: instruments and chemicals, materials syntheses and characterization, photodegradation activity, and antibacterial activity.

#### 3.1 The instruments and chemicals

Following tables are the lists for the instruments and chemicals that we used for synthesis of materials.

Table 3.1 List of the instruments

<b>The characterization techniques</b>	<b>Model</b>
X-ray powder diffractometer (XRD)	DMAX2200/Ultima <sup>+</sup> (Rigaku)
UV-Visible spectrophotometer	HP 8453 (Agilent)
Transmission electron microscope (TEM)	JEM-2100 (JOEL)
Fourier transform infrared spectrometer (FT-IR)	Impact 410 (Nicolet)
X-ray photoelectron spectrometer (XPS)	PHI5000 (ULVAC-PHI)
Dynamic light scattering spectrometer (DLS)	Nano ZSP (Malvern)
Vibrating sample magnetometer (VSM)	Lakeshore model 730908
Scanning electron microscope (SEM)	JSM-IT100 (JEOL)
Inductively coupled plasma-optical emission spectrometer (ICP-OES)	iCAP 6500 (Thermo Scientific)

Table 3.2 List of the chemicals

Chemicals	Suppliers
Iron (III) chloride ( $\text{FeCl}_3$ )	Sigma Aldrich, 97%
Sodium oleate ( $\text{C}_{18}\text{H}_{33}\text{NaO}_2$ )	Sigma Aldrich, $\geq 82\%$
n-Hexane ( $\text{C}_6\text{H}_{14}$ )	ACI Labscan
1-Octadecene ( $\text{C}_{18}\text{H}_{36}$ )	Sigma Aldrich (technical grade)
Oleic acid ( $\text{C}_{16}\text{H}_{34}\text{O}_2$ )	Sigma Aldrich
Ethanol ( $\text{C}_2\text{H}_5\text{OH}$ )	ACI Labscan
Tetraethyl orthosilicate (TEOS)	Sigma Aldrich
Igepal CO-520	Sigma Aldrich
Cyclohexane ( $\text{C}_6\text{H}_{12}$ )	ACI Labscan
Ammonia solution	Merck (for analysis), 25%
1-Hexanol ( $\text{C}_6\text{H}_{14}\text{O}$ )	Sigma Aldrich, 98%
Titanium (IV) butoxide ( $\text{C}_{16}\text{H}_{36}\text{O}_4\text{Ti}$ )	Sigma Aldrich (purum, $\geq 97\%$ )
Hexadecyltrimethyl ammonium bromide ( $\text{C}_{19}\text{H}_{42}\text{BrN}$ , CTAB)	Sigma Aldrich, $\geq 98\%$
<i>N,N'</i> -Dimethylformamide ( $\text{C}_3\text{H}_7\text{NO}$ , DMF)	Sigma Aldrich
Tetra(4-carboxyphenyl)porphyrin (TCPP)	Sigma Aldrich
Copper(II) chloride dihydrate	Sigma Aldrich
Zinc(II) acetate dihydrate	Sigma Aldrich
Iron(III) chloride	Sigma Aldrich
Manganese(II) acetate	Sigma Aldrich
Sodium hydroxide (NaOH)	Merck (pellet for analysis)
Hydrochloric acid (HCl)	Merck
2-Hydroxy-5-sulfosalicylic acid (SSA)	Sigma Aldrich
3-Aminopropyltriethoxysilane (APTES)	Sigma Aldrich
Dicyclohexylcarbodiimide (DCC)	Sigma Aldrich
<i>N</i> -hydroxysuccinimide (NHS)	Sigma Aldrich

### 3.2. Materials syntheses and characterization

To early understand some initial parameters and get enough products for some characterizations, we first synthesized composites between porphyrin and titania

because titania is the outer shell and the active surface of the TSI materials (Section 3.2.1). After we know some initial conditions for the porphyrin attached on titania particles, we then perform experiments for attachment of porphyrin on TSI surface.

### 3.2.1 Synthesis of porphyrin-sensitized titania nanocomposites

Titania nanoparticles were synthesized by reverse microemulsion technique according to previous study [4]. Typically, cetyltrimethylammonium bromide or CTAB (9 g) was dissolved in a mixture of Milli-Q water (3 mL) and 1-hexanol (22 mL). Afterwards, the solution was kept with the continuous stirring at room temperature for 1 h. Tetrabutyl orthotitanate (TBOT) as titanium source (1.5 mL) was injected into the mixed solution under vigorously stirring. The reaction was refluxed at 80 °C with stirring for 24 h. Finally, the as-obtained products were centrifuged and washed three times with water and ethanol, and the obtained titania particles were dried at 50 °C.

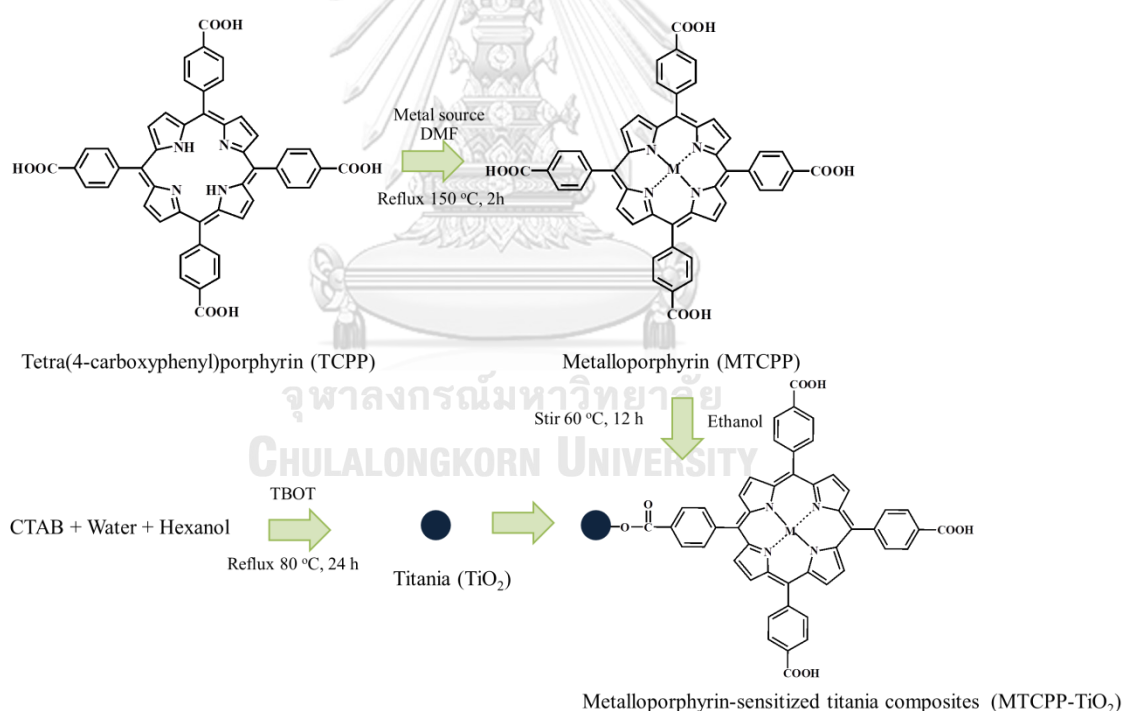


Figure 3.1 Scheme for the synthesis of MTCPP-sensitized titania composites

To study the influence of initial concentration of porphyrin for composite preparation on the photodegradation activity, 1 g of titania nanoparticles were added to the ethanolic solutions containing different concentration of tetra(4-carboxyphenyl)porphyrin (TCPP), 0.4 mM, 1 mM, 4 mM in 10 mL of ethanol. The

mixture was stirred and kept at 60 °C for 12 h. The resulted products were recovered by centrifugation, washed with ethanol and dried at 50 °C for 24 h.

Metalloporphyrins (MTCPPs) with different metal centers were synthesized using tetra(4-carboxyphenyl)porphyrin (TCPP) as free-base porphyrin. 0.033 mmol of TCPP was dissolved in 15 mL of dimethylformamide (DMF). Metal salt (0.182 mmol) was added into solution. The reaction was heated up to 150 °C with continuous stirring and maintained refluxing at 150 °C for 2 h. DMF was removed. To purify metalloporphyrin, the precipitated metalloporphyrin was dissolved in 0.1 M NaOH solution and then centrifuged for separation of impurity. Afterward, the dissolved metalloporphyrin was reprecipitated by adding 1 M HCl solution. MTCPPs were obtained after dissolved in ethanol and dried by evaporation [22, 27, 28]. Below is the list of different metal salts used in the preparation of MTCPPs and the abbreviated names for each metalloporphyrin in our work.

Table 3.3 The abbreviated name for each metalloporphyrins

Metal salts	Metalloporphyrins
Manganese(II) acetate	MnTCPP
Iron(III) chloride	FeTCPP
Copper(II) chloride dihydrate	CuTCPP
Zinc(II) acetate dihydrate	ZnTCPP

### 3.2.2 Synthesis of TSI nanocomposites with different metal centers to study the effect of metal in metalloporphyrin on the photocatalytic performance of the nanocomposites

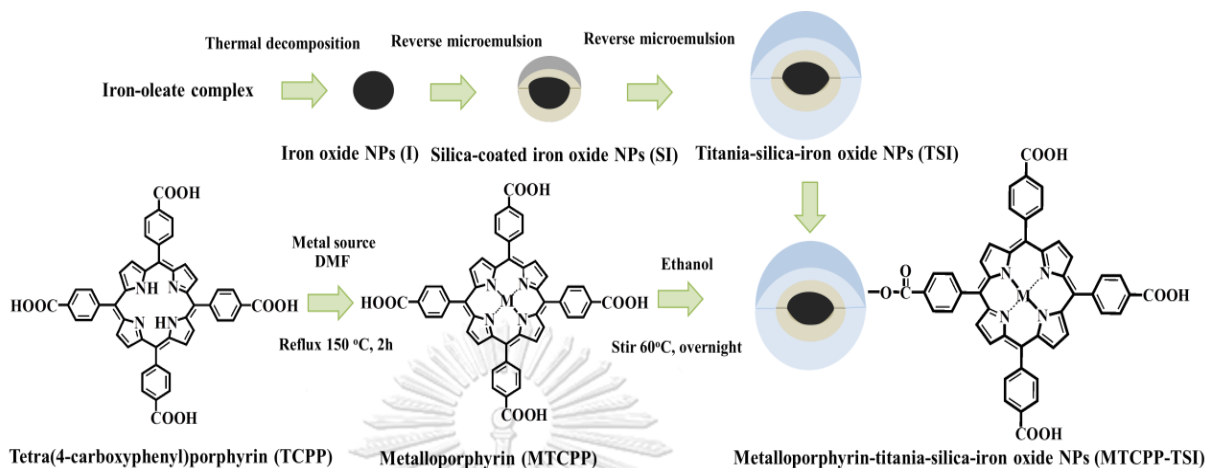


Figure 3.2 Scheme for the synthesis of MTCPP-sensitized TSI nanocomposites [29]

TSI nanocomposites were fabricated according to our previous research [4]. Overall process for the preparation of these nanocomposites is shown in Figure 3.1. In a typical synthesis,  $\text{FeCl}_3 \cdot 6\text{H}_2\text{O}$  as the main precursor and sodium oleate as surfactant were refluxed at 70 °C for 4 h to being iron-oleate complex first. Then, the resulting complex was collected using extraction. The sticky iron-oleate complex, oleic acid and 1-octadecene were mixed together. This mixture was thermally decomposed at high temperature under nitrogen gas flow using the temperature controller. The iron oxide products were precipitated using ethanol before used [10].



Table 3.4 Temperature controlled program for the syntheses of monodisperse iron oxide nanoparticles

Step	Temperature	Time	Note
1	50 °C	0.15 h	Vacuum
2	50 °C	1.00 h	Vacuum
3	320 °C	1.21 h	Feed N <sub>2</sub> (g) when T= 100 ° C
4	320 °C	0.30 h	N <sub>2</sub> gas
5	160 °C	0.05 h	N <sub>2</sub> gas
6	160 °C	2.00 h	Feed O <sub>2</sub> (g)
7	25 °C	0.30 h	-

The SI nanoparticles were prepared *via* reverse microemulsion method using tetraethoxysilane (TEOS) as silicon precursor as shown in the second step in Figure 3.1. First, Igepal CO-520 surfactant was dispersed in cyclohexane, and then the mixture was sonicated for around 10 min. Afterward, iron oxide nanoparticles were added into solution to become a core for these composites. Ammonium hydroxide, which was used as a base catalyst for this reaction, was added into the reaction mixture before TEOS was added. This reaction mixture was incessantly stirred at room temperature for 16 h. The final product was precipitated, washed with ethanol.

After obtaining iron oxide-silica core-shell nanocomposites, the titania coating on the silica composite surface to produce TSI nanocomposites was done using tetrabutyl orthotitanate (TBOT) as titanium precursor [4]. Cetyltrimethylammonium bromide (CTAB) was formed into micelles in hexanol and DI water, before adding TBOT into the solution. This reaction was refluxed at 80 °C for 24 h. After refluxed, the final products were collected washed with the mixed solvent of water and ethanol.

For MTCPP-TSI nanocomposites synthesis, MTCPP complexes with different loadings ranging from 0.002 mmol to 0.02 mmol were dissolved in 5 mL of ethanol solution, and then 50 mg of TSI nanocomposites were added into the solution. The mixture was continuously stirred at 60 °C for 12 h in the dark. MTCPP-TSI was obtained and washed several times with ethanol.

### 3.2.3 Synthesis of TSI nanocomposites with different anchoring groups and the effect of the anchoring group on the photocatalytic performance.

Different methods of attaching MTCPP onto TSI surface were studied. The most suitable methods were determined from photocatalytic activity of the resulted composites. We chose MTCPP-TSI with the best photocatalytic performance from Section 3.2.2. The methods for attaching MTCPP are listed here.

#### 1. The adsorption at room temperature

MTCPP were adsorbed on titania surface of TSI nanocomposites by adopting the procedure reported previously [22]. In this process, 50 mg of TSI nanocomposites were added to MTCPP ethanolic solution (2 mM, 5 mL). The mixture was kept for 3 days at room temperature. The solid was centrifuged and washed with ethanol.

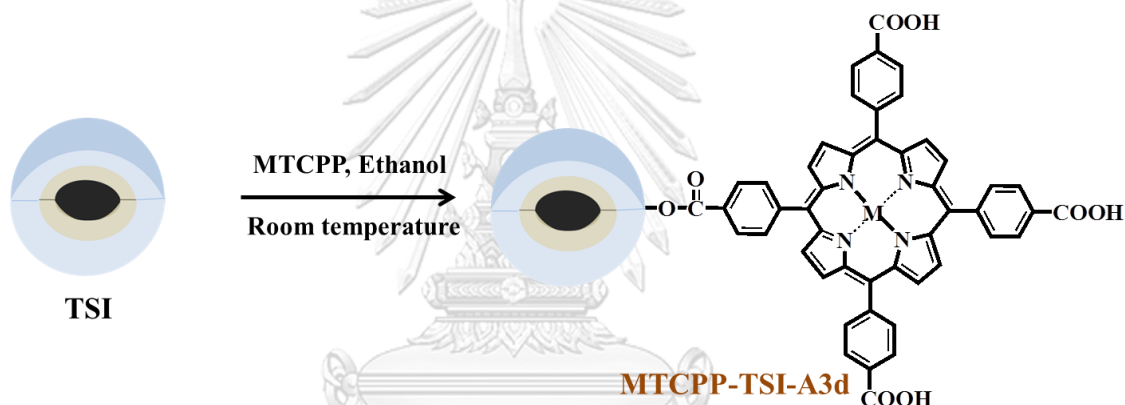


Figure 3.3 Scheme for the synthesis of MTCPP-TSI composites using the adsorption at room temperature

#### 2. The attachment at elevated temperature [22]

2 mM MTCPP complexes were dissolved in 5 mL of ethanol solution, and then TSI nanocomposites (50 mg) were added into solution. The mixture solution was continuously stirred at 60 °C for 12 h. The products (MTCPP-sensitized TSI nanocomposites) were collected and washed with ethanol.

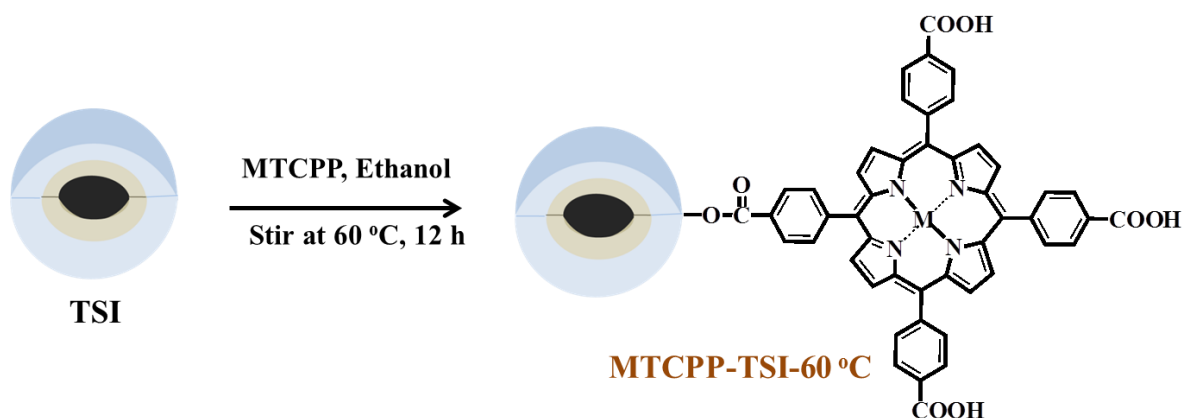


Figure 3.4 Scheme for the synthesis of MTCPP-TSI composites using stirring at 60 °C

3. The covalent attachment using 2-hydroxy-5-sulfosalicylic acid (SSA) as a bridging molecule [19]

2-hydroxy-5-sulfosalicylic acid (SSA) (3mmol) was dissolved in dioxane (5 mL). 50 mg of TSI nanocomposites were added into solution. The reaction mixture was stirred at 80 °C for 2h. The TSI with SSA composites were centrifuged to separate them from the reaction mixture. TSI with SSA nanocomposites were refluxed at 80 °C for 24 h with metalloporphyrin complexes. The final product was washed with dioxane and ethanol.

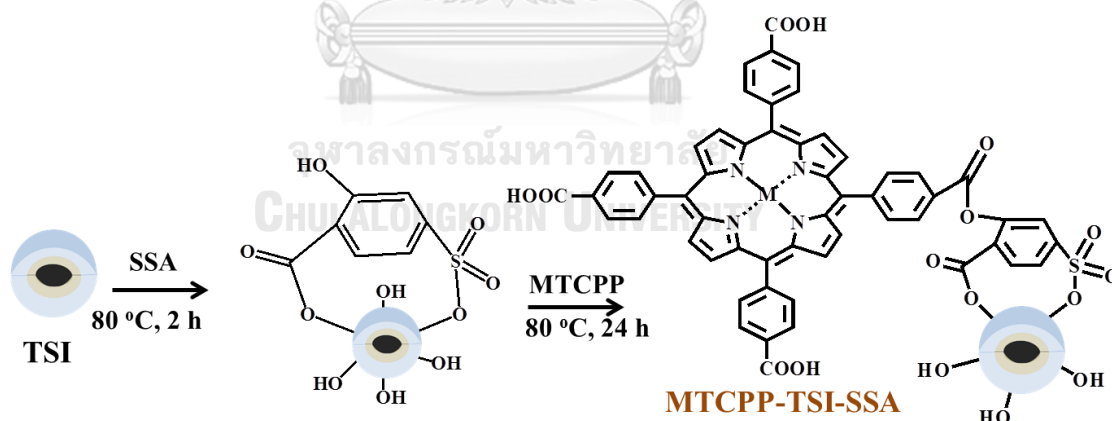


Figure 3.5 Scheme for the synthesis of MTCPP-TSI composites using the 2-hydroxy-5-sulfosalicylic acid (SSA) as a bridging molecule

4. The covalent attachment using 3-aminopropyltriethoxysilane (APTES) as a bridging molecule [23, 30]

The surface of titania is coated with 3-aminopropyltriethoxysilane (APTES) by silane-coupling reaction. 50 mg of TSI nanocomposites were mixed with

anhydrous toluene (50 mL) using magnetic stirrer. The mixture was refluxed at 110 °C under nitrogen atmosphere with continuously stirring. Then, 1.5 mL of APTES was injected into solution using a syringe. The reaction mixture was kept at 110 °C under nitrogen gas for 24 h. Then, the obtained APTES-immobilized TSI nanoparticles were collected. MTCPP and APTES-immobilized TSI nanoparticles were coupled using DCC coupling method. 0.066 mmol of dicyclohexylcarbodiimide (DCC), 7.6 mg of *N*-hydroxysuccinimide (NHS) and 0.01 mmol MTCPP were mixed in DMF 5 mL. The reaction was stirred for 3h under nitrogen gas. The amine conjugated titania-silica-iron oxide composites (TSI-NH<sub>2</sub>) were contained in a three neck round bottom flask under nitrogen flowing. The metalloporphyrin solution was injected into the flask and continuously stirred under nitrogen atmosphere for 24 h.

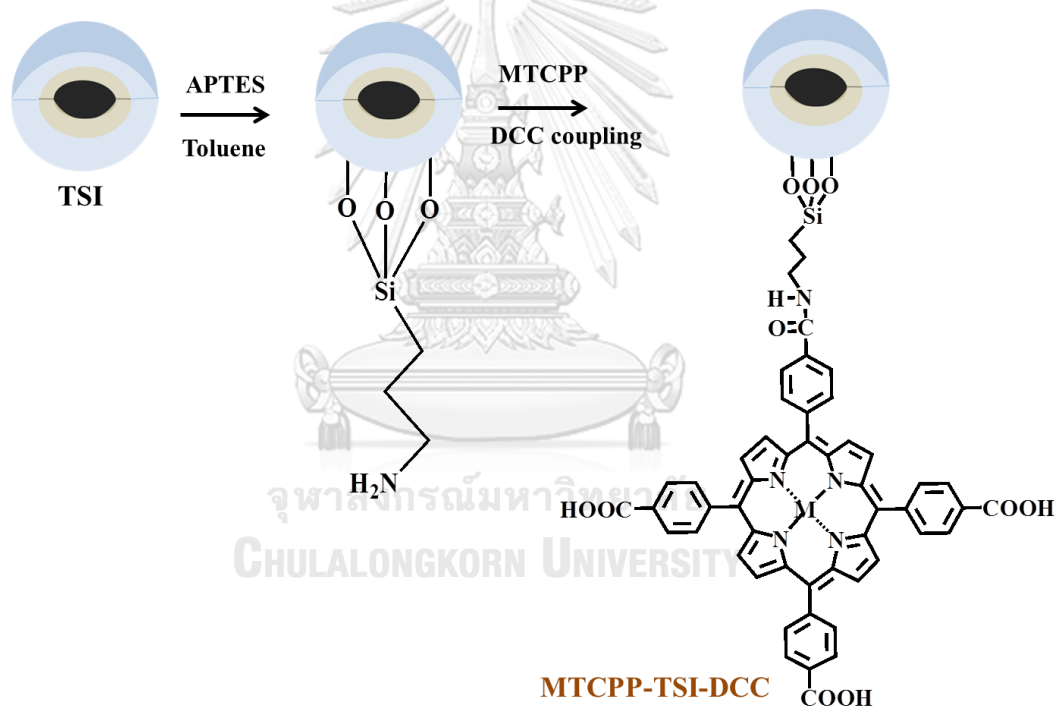


Figure 3.6 Scheme for the synthesis of MTCPP-TSI composites using the covalent attachment

### 3.3 Characterization of the as-synthesized nanocomposites

UV-visible absorption spectra of solutions were determined on a HP 8453 (Agilent, USA) UV-vis spectrophotometer. The absorption spectra were used to confirm the metalation of porphyrin. Moreover, the MB solution samples from

photocatalytic degradation were taken at pre-determined time intervals and analyzed using this instrument.

The Fourier transforms infrared spectroscopy (FT-IR) spectra were performed by a Nicolet 6700 FTIR spectrometer operating in the range of 400-4000  $\text{cm}^{-1}$ . The spectra were recorded using transmission mode to confirm the functional group. A mixture of sample and dried KBr powder was compressed into a pellet before measuring.

X-ray diffraction patterns were recorded using a D/MAX 2200 X-ray diffractometer (Rigaku, Japan) with an incident  $\text{Cu-K}\alpha$  radiation over a 2-theta in a range of  $20^\circ$  to  $70^\circ$ . An accelerating voltage and an applied current were kept at 40 kV and 30 mA, respectively. They were used on the identification of the crystal structure and phase composition.

Transmission electron microscopy (TEM) images were carried out using a JEOL 2100 microscope at a 120 kV accelerating voltage (Japan). A small amount of product dispersed in ethanol was prepared to be a drop of colloidal solution using ultrasonic treatment for a few min. It was drop-casted onto a grid and dried using a desiccator before TEM analysis. The images were used to investigate about the thickness of coating of both the layers and the size of particles. The selected area electron diffraction pattern (SAED) was obtained on a Hitachi transmission electron microscope (HT7700).

The X-ray photoelectron spectrometer (XPS) was observed using PHI5000 Versa Probe II (ULVAC-PHI, Japan) equipped with monochromated Al  $\text{K}\alpha$  radiation, and the binding energies were corrected using carbon ( $\text{C1s}$  at 284.6 eV) as a reference.

The vibrating sample magnetometer (VSM) (Lakeshore model 730908, USA) was used to measure the magnetization of samples. It was carried out at room temperature. This system was calibrated with a nickel sphere.

Dynamic light scattering (DLS) analysis was used to determine the hydrodynamic size distribution of the dispersed nanocomposites in PBS buffer at pH 7.4. As-synthesized nanocomposite hydrodynamic size distributions were measured using a Malvern Zetasizer Nano ZSP. All of DLS analysis was carried out at room temperature.

The scanning electron microscope (SEM) images and energy-dispersive X-ray (EDX) images of the photocatalysts were obtained by a JEOL (JSM-IT100), with an operating voltage of 20 kV. The as-prepared nanocomposites characteristics such as morphology were determined.

UV-Vis spectra of sample in solid phase were done using Shimadzu UV-Visible spectrophotometer (UV-2550).

The inductively coupled plasma-optical emission spectrometer (ICP-OES) analyses were taken by Thermo Scientific (iCAP 6500). It was used to determine elemental content of the sample solution after each reused cycle.

### **3.4 Photocatalytic degradation measurement**

#### **3.4.1 The effect of metal centers in porphyrin on the photocatalytic degradation performance under visible irradiation**

The photocatalytic activities of MTCPP-TSI nanocomposites were comparatively evaluated by measuring the photocatalytic degradation of methylene blue (MB) solution under visible light irradiation in comparison to the TSI nanoparticles. For photocatalytic degradation experiment, 10 mg of each photocatalyst was dispersed in a 30 mL aqueous media (pH 7) of 7 ppm MB. The mixture was kept in a dark chamber under stirring for 1 h to ensure the establishing of an adsorption-desorption equilibrium, water and the dye before irradiation. Afterward, the suspension was exposed to visible light from a 100W incandescent lamp. At specific time intervals of visible light irradiation, the decrease of the MB absorbance at 664 nm was carried out and analyzed by UV-Vis absorption spectroscopy. The photocatalyst was removed from the methylene blue solution using a magnet [4].

#### **3.4.2 The effect of anchoring group between porphyrins and titania on the photocatalytic degradation performance under visible irradiation**

The different anchoring group samples were investigated in the MB photodegradation activity using the procedure corresponding to the study in the effect of metal center in porphyrin in 3.4.1.

### 3.4.3 Reusability of the nanocomposites

The reusability of the highest efficiency photocatalyst was investigated by repeating the photocatalytic cycles at the same procedure (3.4.1). The reused catalyst was collected from media using a magnet before the next cycle. The repeated photocatalytic cycle was done for six times.

### 3.4.4 The effect of MB concentration on the photocatalytic degradation performance under visible irradiation

Various concentrations of methylene blue ranging from 5 ppm to 15 ppm were used to investigate photooxidation activity. In each testing, the loading of photocatalysts was kept constant at 10 mg to degrade 30 mL of MB solution within 3 h of visible light irradiation.

## 3.5 Antibacterial activity

The bacteria killing activity was conducted as previous described with small modification [4, 31]. *E. coli* cells were cultured in Luria-Bertani (LB) broth at 37 °C with shaking for overnight. Then, the overnight cultures were adjusted to OD<sub>600 nm</sub> of 0.1 in a fresh LB broth and incubated at the same conditions until bacterial cells reached log phase (an absorbance of bacterial suspension at 600 nm of 0.5). The log phase cells were then harvested by centrifugation at 7000 rpm for 10 min. After that, these harvested cells were suspended in normal saline (0.9% sodium chloride) at equal volume of bacterial culture. The *E. coli* cells were treated with two concentrations, including 17.5 and 20 mg/L of the best magnetic nanocomposites from our study. The suspensions were illuminated at 37 °C for 3 h by a 100W incandescent lamp. The serial dilution on LB agar was done after 3h of irradiation. The viable cells were scored as colony-forming units (CFU) after incubation at 37 °C for overnight. The viable cell count method was used to enumerate survival cells. The *E. coli* cells untreated under irradiation were conducted in parallel with tested experiments and used as a control experiment. All experiments were repeated for at least three times. In addition, non-activated conditions were performed along with all experiments to investigate the photocatalytic killing activity of nanocomposites.

## CHAPTER IV

### RESULTS AND DISCUSSION

In this work, the magnetic nanocomposites were prepared and characterized. The photodegradation activities and antibacterial activities under visible light activation were then evaluated.

#### 4.1 Characterization of metalloporphyrin-sensitized titania particles and their photodegradation results

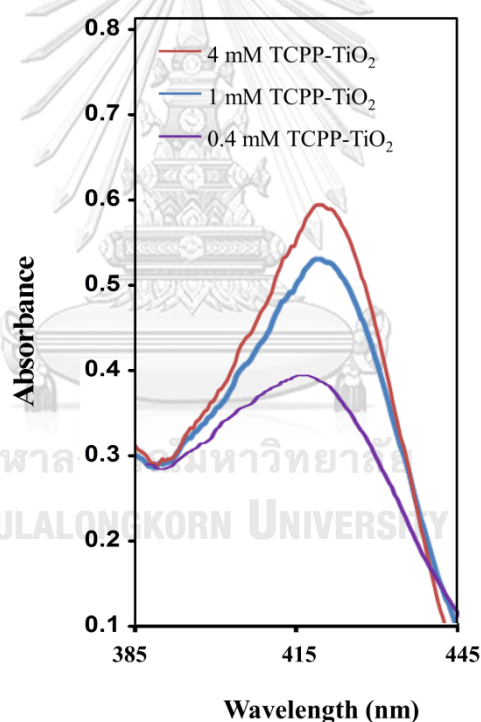


Figure 4.1 DR-UV spectra of TCPP-TiO<sub>2</sub> samples

The diffuse reflectance spectroscopy is an efficient and powerful method to determine the presence of porphyrin. To study the effect of initial concentration of TCPP for preparation porphyrin-TiO<sub>2</sub> samples, as shown in the DR-UV spectra (Figure 4.1), all TCPP-TiO<sub>2</sub> samples exhibited the highest absorption peak falling in



visible region. The increase in absorbance of TCPP on composite was observed when the initial concentration of TCPP increased.

Nitrogen adsorption-desorption isotherms are revealed in Figure 4.2, and the calculated specific surface area are summarized in Table 4.1 for all TCPP-TiO<sub>2</sub> composites. The overall shape of the nitrogen adsorption-desorption isotherms for TCPP-TiO<sub>2</sub> samples indicated Type IV isotherm in the IUPAC classification as the hysteresis loop at the relative pressure from 0.4 to 0.8 exhibited mesoporous characteristics. The specific surface area of pure TiO<sub>2</sub>, 0.4 mM TCPP-TiO<sub>2</sub>, 1 mM TCPP-TiO<sub>2</sub> and 4 mM TCPP-TiO<sub>2</sub> was 236.19, 237.09, 232.20 and 174.58 m<sup>2</sup> g<sup>-1</sup>, respectively. The results show that the specific surface area for 0.4 mM TCPP-TiO<sub>2</sub> sample was similar to that of the neat TiO<sub>2</sub> as a small amount of TCPP adsorbed on TiO<sub>2</sub> did not affect the overall surface area. The specific surface area of 1mM TCPP-TiO<sub>2</sub> and 4 mM TCPP-TiO<sub>2</sub> decreased compared to that of the pure TiO<sub>2</sub> due to the incorporation of TCPP after modification on TiO<sub>2</sub> surface [32]. This result can support that TCPP was attached on TiO<sub>2</sub> surface.

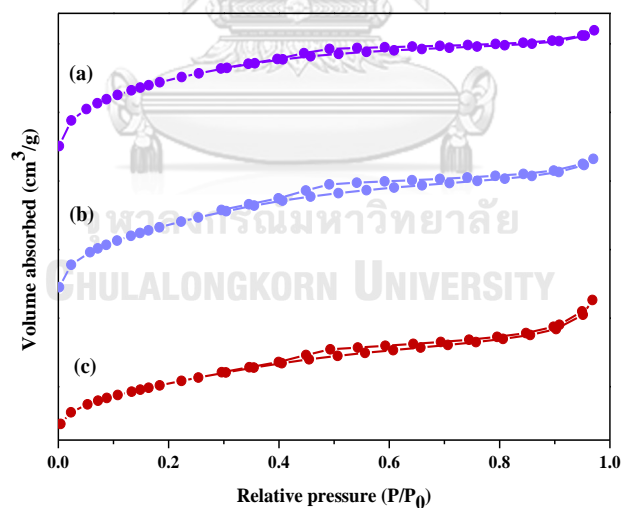


Figure 4.2 The nitrogen adsorption-desorption isotherms of (a) 0.4 mM TCPP-TiO<sub>2</sub>, (b) 1 mM TCPP-TiO<sub>2</sub>, (c) 4 mM TCPP-TiO<sub>2</sub>

Table 4.1 Specific surface area values of TCPP-TiO<sub>2</sub> samples

Sample	Surface area (m <sup>2</sup> g <sup>-1</sup> ) <sup>a</sup>
Pure TiO <sub>2</sub>	236.19
0.4 mM TCPP-TiO <sub>2</sub>	237.09
1 mM TCPP-TiO <sub>2</sub>	232.20
4 mM TCPP-TiO <sub>2</sub>	174.58

<sup>a</sup> Specific surface area data calculated from the multi-point BET method.

#### 4.1.1 Effects of metal center in porphyrin on the photocatalytic degradation performance under visible irradiation

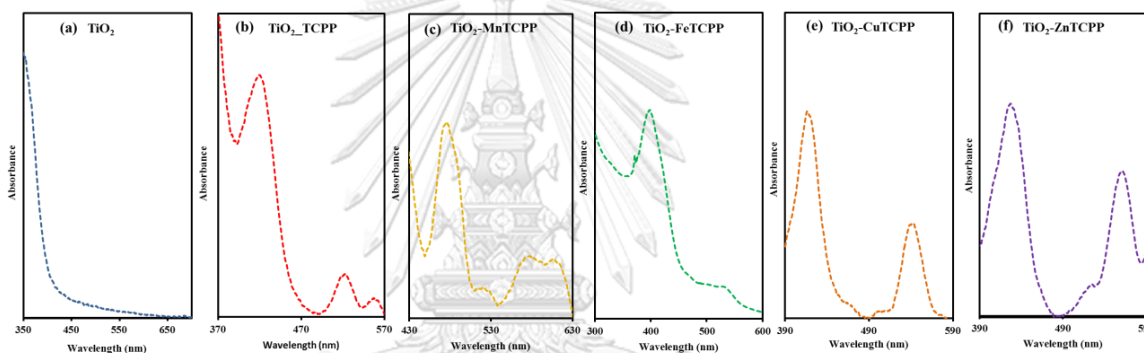


Figure 4.3 The DR-UV spectra of MTCPP-TiO<sub>2</sub> sample with the different metal centers or free-base compared to TiO<sub>2</sub>.

The UV-Vis diffuse reflectance spectra of the products of various porphyrins attached on TiO<sub>2</sub> exhibited an obvious absorbance in the region of visible light compared with the neat TiO<sub>2</sub>. It could suggest that the new absorption band can increase in the light-harvesting ability within visible irradiation [22].

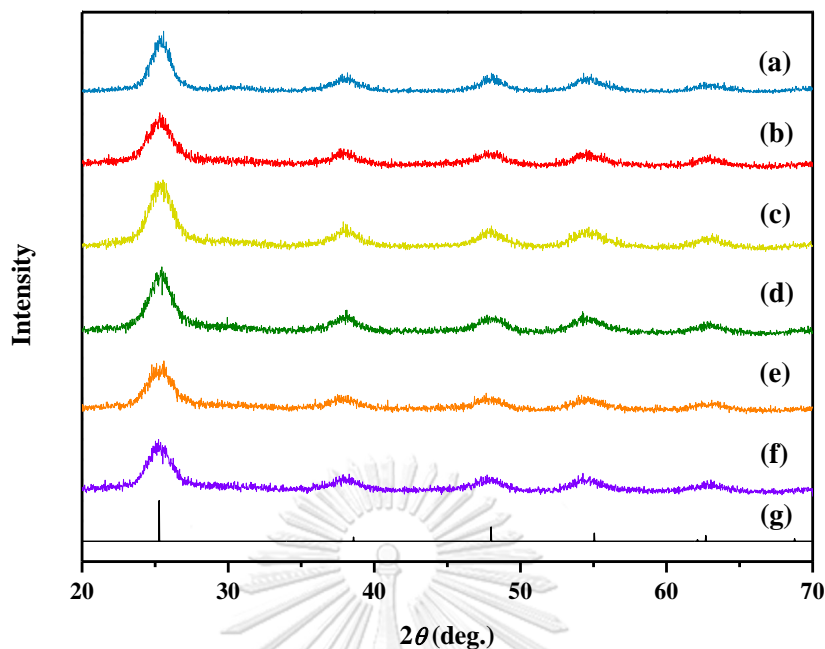


Figure 4.4 XRD patterns of (a)  $\text{TiO}_2$ , (b)  $\text{TCPP-TiO}_2$ , (c)  $\text{MnTCPP-TiO}_2$ , (d)  $\text{FeTCPP-TiO}_2$ , (e)  $\text{CuTCPP-TiO}_2$ , (f)  $\text{ZnTCPP-TiO}_2$ , (g) JCPDS no. 21-1272

The XRD patterns of metalloporphyrin-sensitized titania composites (MTCPP- $\text{TiO}_2$ ), metal-free porphyrin-sensitized titania composites (TCPP- $\text{TiO}_2$ ) and titania particles were observed as shown in Figure 4.4. All the diffraction peaks in pure titania XRD pattern are identified as the anatase phase according to JCPDS no.21-1272 [4]. The XRD patterns of MTCPP- $\text{TiO}_2$  with different metal addition and TCPP- $\text{TiO}_2$  are similar to that of the bare  $\text{TiO}_2$ . It is clearly observed that the modification of porphyrin has no influence on the phase structure of the bare  $\text{TiO}_2$ .

Firstly, the photocatalytic activities of various concentrations of TCPP that were deposited onto titania nanoparticles are exhibited in Figure 4.5. Among three concentrations, TCPP- $\text{TiO}_2$  with the concentration of 4 mM exhibited the best condition for photodegradation. It can be indicated that the increase in initial concentration of porphyrin will affect the amount of porphyrin on materials, and finally it will mainly affect the photocatalytic results.

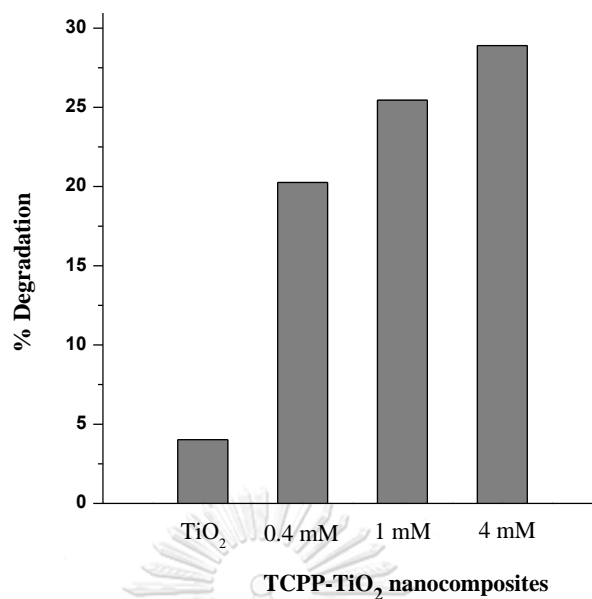


Figure 4.5 The photodegradation of MB using various TCPP-TiO<sub>2</sub> samples and the bare TiO<sub>2</sub>

Secondly, we studied the photodegradation of MB with different metal centers on porphyrin compared with the bare TiO<sub>2</sub> (Figure 4.6). The ratio between the added porphyrin and TiO<sub>2</sub> was 0.04 mmol MTCPP/1g TiO<sub>2</sub>. The photodegradation based on the same amount of catalysts increased in the order of CuTCPP-TiO<sub>2</sub> > ZnTCPP-TiO<sub>2</sub> > MnTCPP-TiO<sub>2</sub>, FeTCPP-TiO<sub>2</sub> > TCPP-TiO<sub>2</sub> > TiO<sub>2</sub>. In pure TiO<sub>2</sub>, it did not show any absorption peak in visible region.

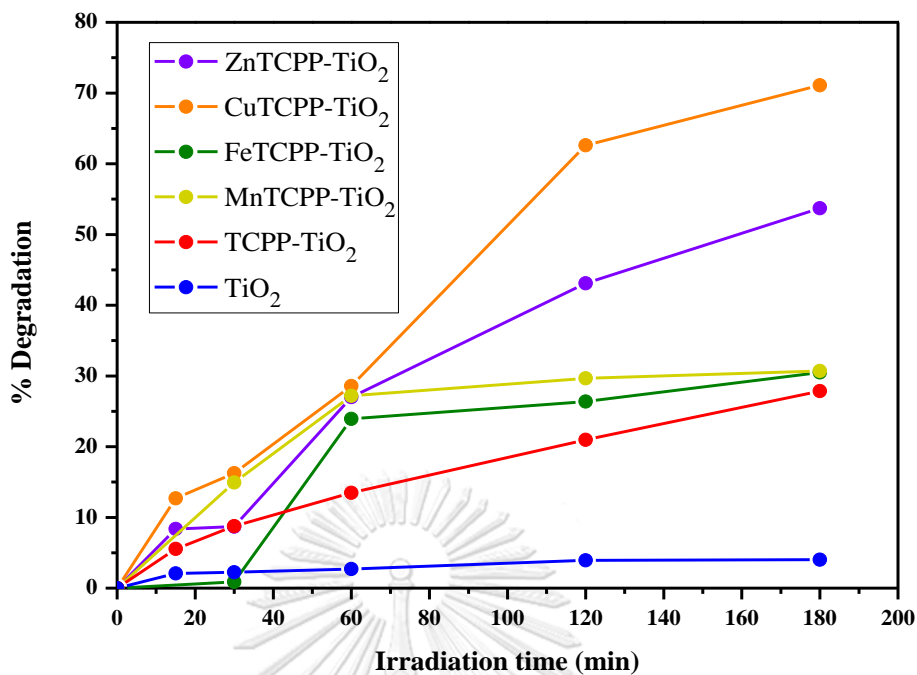


Figure 4.6 The photodegradation of MB using MTCPP-TiO<sub>2</sub> samples

## 4.2 Characterization of metalloporphyrin-sensitized TSI nanocomposites and their photodegradation results

### 4.2.1 Effects of metal center in porphyrin on the photocatalytic degradation performance under visible irradiation

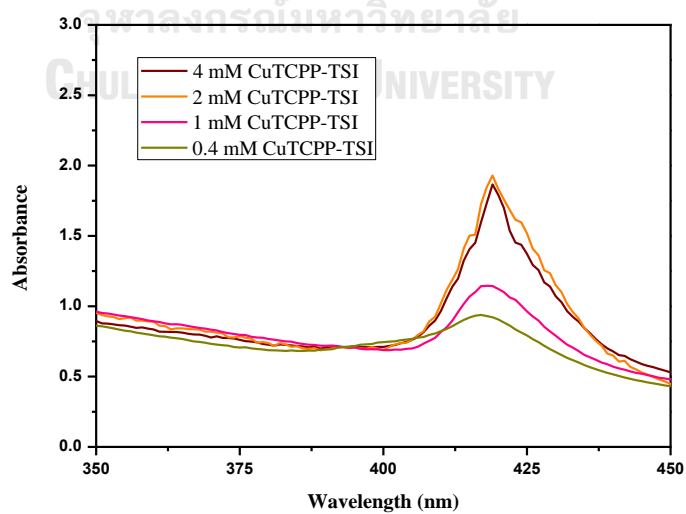


Figure 4.7 The UV-vis spectra of CuTCPP-TSI samples

From the DR-UV results of TCPP-TiO<sub>2</sub> samples above, the initial porphyrin concentration exhibited the effect on the enhancement in absorbance for the as-prepared product. To find the suitable initial metalloporphyrin concentration for metalloporphyrin-TSI composites synthesis, the spectra of TSI composites with different CuTCPP concentrations are shown in Figure 4.7. We selected the CuTCPP as a model because it is the best photocatalyst in metalloporphyrin-TiO<sub>2</sub> composites as shown in Figure 4.6. It can be noticed that the enhanced absorbance for 2 mM CuTCPP-TSI sample was similar to that of 4 mM CuTCPP-TSI sample, suggesting that 2 mM of CuTCPP is the suitable initial concentration of metalloporphyrin for further syntheses.

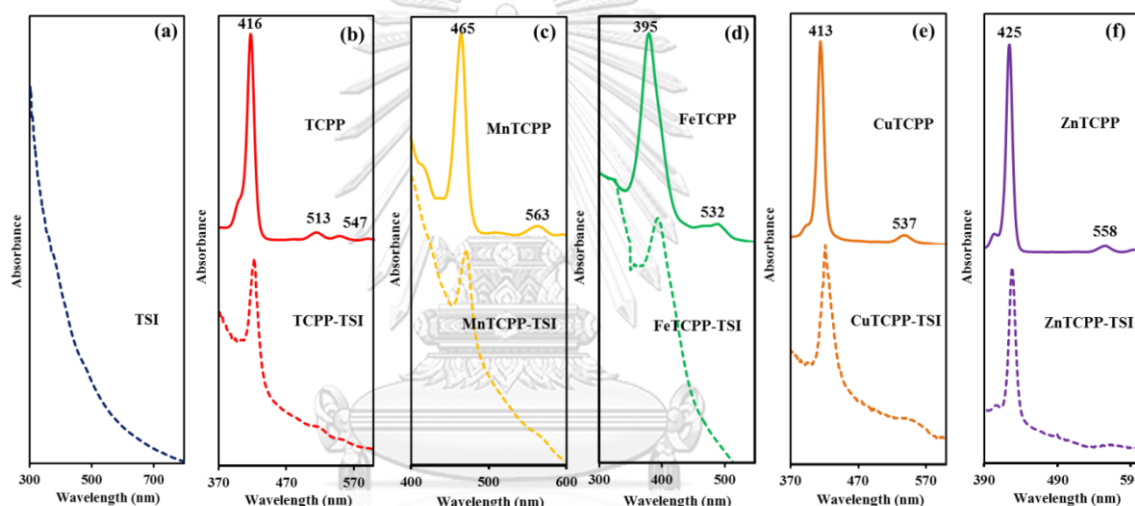


Figure 4.8 UV-Vis absorption spectra of (a) TSI, (b) TCPP and TCPP anchored on TSI, (c) MnTCPP and MnTCPP anchored on TSI, (d) FeTCPP and FeTCPP anchored on TSI, (e) CuTCPP and CuTCPP anchored on TSI, and (f) ZnTCPP and ZnTCPP anchored on TSI nanocomposites

The metalation reaction on porphyrin was identified using the different spectrophotometric properties of porphyrins. The maxima UV-vis absorption band of metal-free porphyrin (TCPP) and metalloporphyrins (MTCPPs) are shown in Figure 4.8. Porphyrins exhibited the characteristic peaks of two  $\pi \rightarrow \pi^*$  electronic transition in visible region. The electronic transition from  $a_{1u}(\pi)$  to  $e_g^*(\pi)$  and  $a_{2u}(\pi)$  to  $e_g^*(\pi)$  in porphyrin structure are the Soret band and Q band, respectively [22]. The strong Soret band or B band of free-base porphyrin (TCPP) in ethanol is observed at 416 nm, and

four Q bands are detected in visible spectrum. Metals in the cavity of porphyrin affect the shift to a higher or shorter wavelength of the B band of TCPP.

Changing the absorption features, both intensity and wavelength, is caused by the insertion of various transition metals into the TCPP [16]. In the coordination, N atoms on a ligand donate the lone pair electrons to metal center, and ligand accepts electrons from the metal center, so the delocalized  $\pi$  bonds are formed. The Soret absorption band of CuTCPP and FeTCPP are blue shifted with respect to free base porphyrin (TCPP) which agrees well with the previous report [22]. The blue shift in the UV-Vis absorption spectra when Fe(III) and Cu(II) are substituents in porphyrin are resulted from the in-plane metalloporphyrins. As the critical size of Fe(III) and Cu(II) ions are suitably inserted into the cavity of the porphyrin ligand, so the atomic orbitals of the metal centers can overlap more strongly with the ligand at highest occupied molecular orbitals (HOMO), resulting in the reduction in the level of HOMO. No change occurs in level of the lowest unoccupied molecular orbitals (LUMO). Hence, the increase in energy gaps of the ligand in CuTCPP and FeTCPP leads to a decrease in the absorption wavelength signals (blue shift). On the contrary, the Soret absorption bands of MnTCPP and ZnTCPP present a red shift compared to metal-free porphyrin (TCPP) [16]. The red shifted UV-Vis absorption bands of Mn(II) and Zn(II) in the porphyrin cavity represented in the out-of-plane metalloporphyrins, which are borderline metalloporphyrins. The weaker interaction between the atomic orbitals of the metal centers and the HOMO has no effect on the energy level of HOMO, but it affects mainly for the energy level of LUMO in the out-of-plane metalloporphyrins. The increase in the wavelengths comes from the interaction of the unchanged HOMO and lower LUMO energy level [16].

The UV-Vis absorption spectra of colloidal MTCPP-TSI nanocomposites and TSI nanocomposite are presented in dash line in Figure 4.8. TSI nanocomposite showed the spectrum without any peak in visible region, while MTCPP-TSI nanocomposites spectra revealed similar characters to those of the corresponding free metalloporphyrins spectra. Furthermore, a small red shift compared to free porphyrins is likely due to the graft of porphyrins on the TSI nanocomposites surface through the carboxylate group corresponding to electronic coupling between porphyrins and titania surface. Metalloporphyrin-sensitized TSI nanocomposites (MTCPP-TSI)

should be a better photocatalyst under sunlight than the TSI magnetic nanocomposites because they contained a new absorption signal that falls in the range of the solar spectrum. The absorption spectra of the MTCPP-TSI nanocomposites suggested that all nanocomposites could use visible light for activating the catalyst to provide a photocatalyst with extended absorption spectra in visible-light region.

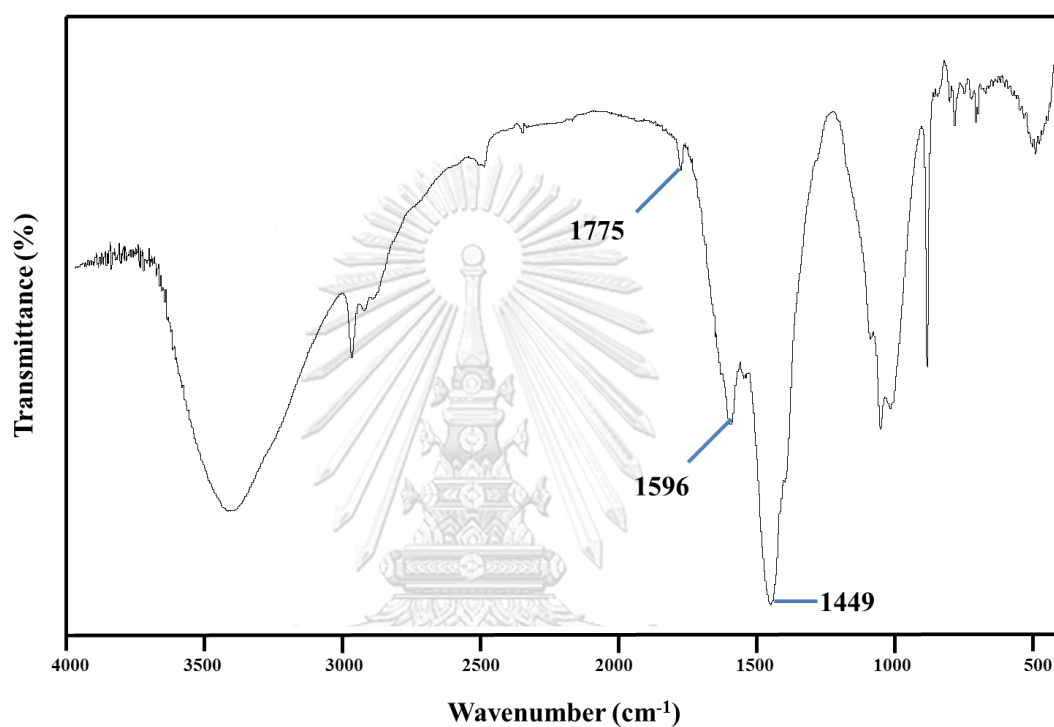


Figure 4.9 FT-IR spectrum of CuTCPP

CHULALONGKORN UNIVERSITY



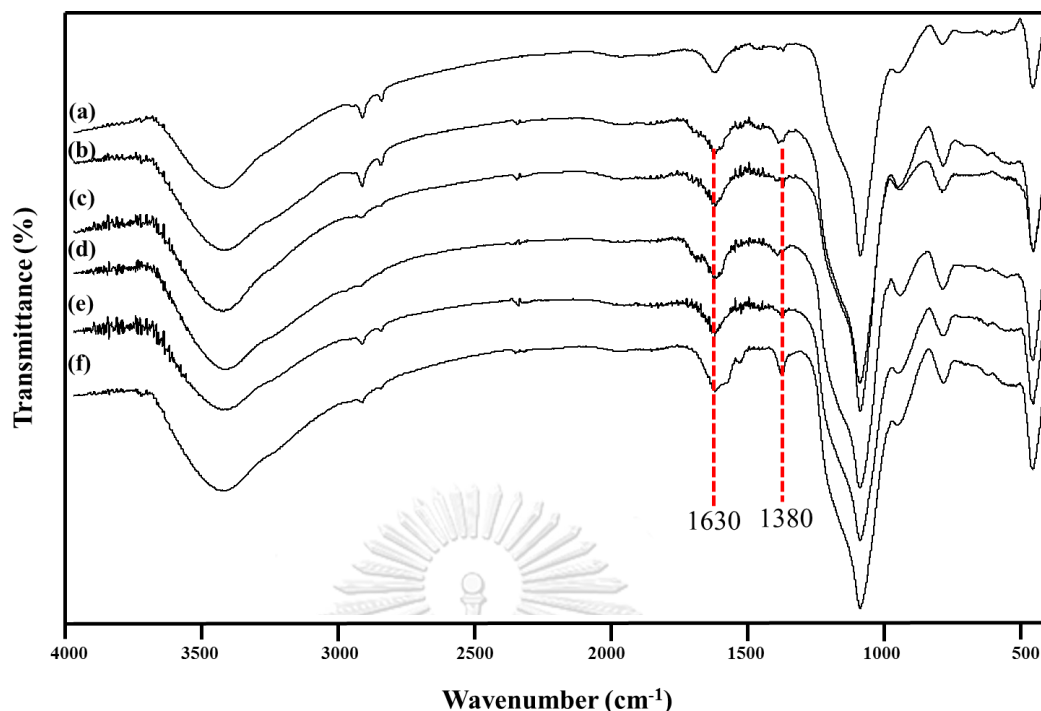


Figure 4.10 FT-IR spectra of (a) TSI composites, (b) TCPP-TSI composites, (c) MnTCPP-TSI composites, (d) FeTCPP-TSI composites, (e) CuTCPP-TSI composites, (f) ZnTCPP-TSI composites

FT-IR spectrum of CuTCPP exhibited the vibration at  $1775\text{ cm}^{-1}$ , which was attributed to the stretching of C=O of carboxylic acid [33-35]. The asymmetric (overlap with stretching of C=C bond of porphyrin [35]) and symmetric stretching of  $\text{-COO}^-$  can be observed at  $1596$  and  $1449\text{ cm}^{-1}$ [33, 34].

IR spectroscopy is used for better understanding the interaction between TSI nanocomposites and metalloporphyrin complexes by comparing the bonds in TSI nanocomposites and MTCPP-TSI nanocomposites. TSI magnetic composites showed stretching signal at  $3440\text{ cm}^{-1}$  corresponding to O-H stretching of titania (Figure 4.10a). The bending vibration of O-H group on the composite surface can be observed at  $1627\text{ cm}^{-1}$ [33]. The absorption band at  $1101\text{ cm}^{-1}$  was attributed to the asymmetric Si-O-Si stretching band [4, 23]. The band at  $467\text{ cm}^{-1}$  was assigned to the stretching vibration peak of Ti-O-Ti band [4]. For FT-IR spectra of MTCPP-TSI nanocomposites as shown in Figure 4.10 (b-f), all the signals belong to TSI nanocomposites still appeared corresponding to the bonds in titania and silica. The presence of the porphyrins on the composite surface resulted in two new extra peaks.

The symmetric and asymmetric (overlap with the O-H bending vibration) stretches of  $\text{-COO}^-$  that associated with the porphyrin were found at  $1380$  and  $1630\text{ cm}^{-1}$  [19, 22, 23, 32, 35]. The presence of carboxylate group suggested that both metal-free porphyrin and metalloporphyrin complexes were successfully chemisorbed as carboxylate species on the TSI magnetic composites surface.

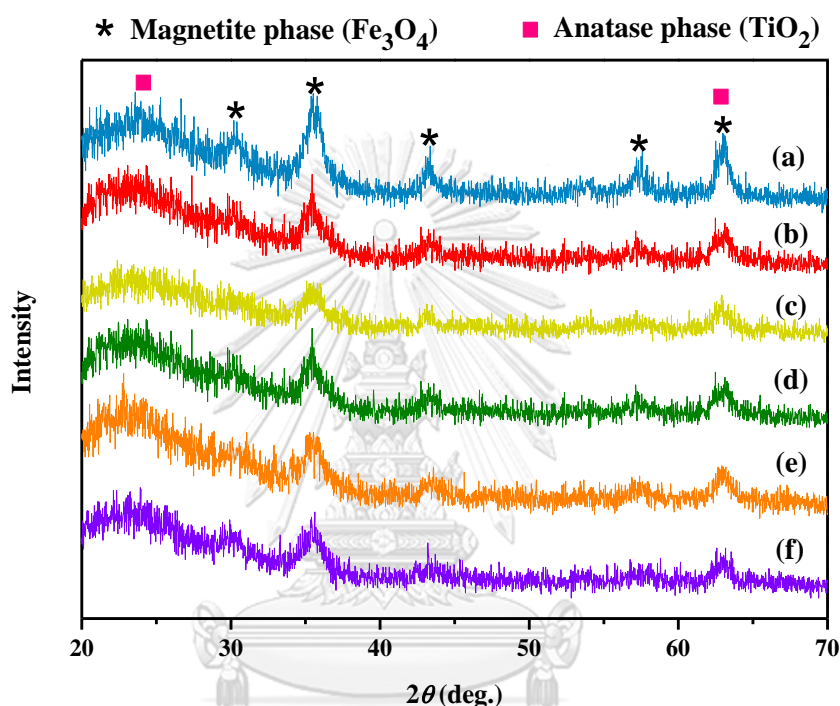


Figure 4.11 X-ray diffraction patterns of (a) TSI composites, (b) TCPP-TSI composites, (c) MnTCPP-TSI composites, (d) FeTCPP-TSI composites, (e) CuTCPP-TSI composites, (f) ZnTCPP-TSI composites

XRD patterns of TSI and MTCPP-TSI exhibited the crystal structures as shown in Figure 4.11. The XRD pattern of TSI nanocomposites is consistent with the strong diffraction signals from magnetite phase of iron oxide (JCPDS no. 19-0629) and weaker diffraction signals from anatase phase of titania (JCPDS no. 21-1272) [4]. The results suggest that the TSI nanocomposites had the crystal phase of iron oxide higher than that of anatase titania, while the amorphous silica interlayer did not appear as any sharp peaks. After TSI nanocomposite underwent surface modification with porphyrins, they did not exhibit any shifts in the characteristic diffraction peaks in all composites in XRD patterns. This observation indicates that the surface modification

did not alter the crystal structure of TSI nanocomposites. In addition, all XRD patterns of MTCPP-TSI nanocomposites revealed no diffraction peaks from metalloporphyrin molecules, suggesting that the metalloporphyrins stayed as a thin layer adsorbed on TSI surface rather than stayed as separated phases. As the XRD studies, it can be indicated that MTCPP-TSI composites not only still have the ferrimagnetic property of magnetite phase, but also have the photocatalytic property from the anatase titania phase. Furthermore, the Debye-Scherrer equation was used to calculate the crystalline size from the (3 1 1) crystal plane of magnetite (parent peak). The estimated crystalline sizes of all nanocomposites were found as shown in Table 4.2. Based on the result, the crystalline size falls in the range of 5.33–6.28 nm, confirming that the presence of metalloporphyrins and the synthesis process did not much affect the crystalline size of magnetic nanoparticles inside composites.

Table 4.2 The estimated crystalline sizes of magnetite calculated using the Debye-Scherrer equation from the full width at half maximum (FWHM) from the XRD patterns in Figure 4.11.

Sample	Crystalline sizes (nm)
TSI	6.28
TCPP-TSI	6.00
MnTCPP-TSI	6.15
FeTCPP-TSI	6.00
CuTCPP-TSI	5.95
ZnTCPP-TSI	5.33

The Debye-Scherrer equation for calculation:  $D = 0.9\lambda/(\beta \cos \theta)$

D = Particle sizes

$\lambda = 1.54060 \text{ \AA}$  in the case of  $\text{CuK}_{\alpha 1}$

$\beta$  = the full width at half maximum intensity of the peak (in Rad)

$\theta$  = theta

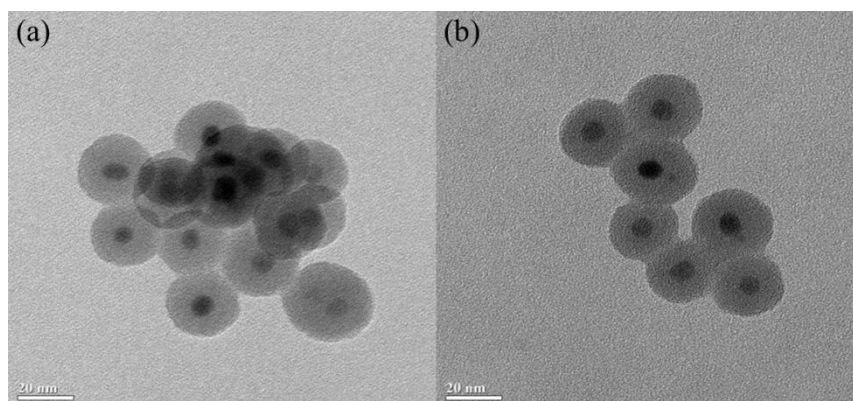


*Figure 4.12 The TEM images of (a) TSI nanocomposites and (b) CuTCPP-TSI nanocomposites*

TEM images are used to characterize the morphology and sizes of the nanocomposites in comparing between TSI and CuTCPP-TSI nanocomposites. From TEM image of TSI in Figure 4.12a, TSI nanocomposites presented a monodisperse core-shell structure as has been studied in our previous study [4]. The iron-oxide core (dark gray) had a mean diameter of about 8–10 nm. The shell consisted of silica interlayer and titania layer (gray shell) that were completely coated onto the iron oxide nanoparticles. After the composite has undergone the surface modification with CuTCPP, TEM image of CuTCPP-TSI nanoparticles (Figure 4.12b) still displayed uniform spherical shape with an average diameter of about 26.5 nm. It can be seen that both nanocomposites did not reveal particle aggregation, and they presented similar sizes and structures. In addition, the selected area electron diffraction pattern of CuTCPP-TSI as shown in Figure 4.13 reveals the five distinct ring patterns that are characteristic of the magnetite crystallites. The d-spacings in our results were 0.149, 0.162, 0.121, 0.255, 0.291 nm that can be identified to (440), (511), (400), (311), (220) crystal planes, respectively. They matched well with the major d-spacings of magnetite phase and agreed with the XRD results (JCPDS no.19-0629). All TEM results of CuTCPP-TSI nanoparticles revealed that the modification of TSI with copper-porphyrin did not have influence the structure, size and the aggregation of the composites. These composites still reveal planes in TEM-SAED result according to magnetite phase from XRD.

Table 4.3 The calculated d-spacings of CuTCPP-TSI measured using TEM-SAED technique.

d-spacings (nm) (TEM-SAED)	d-spacings (nm) (XRD database)	Crystal plane
0.149	0.14845	(440)
0.162	0.16158	(511)
0.212	0.20993	(400)
0.255	0.25320	(311)
0.291	0.29670	(220)

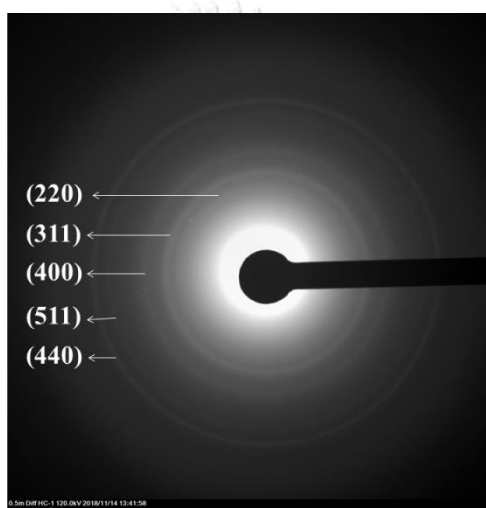


Figure 4.13 The selected area electron diffraction pattern of CuTCPP-TSI nanocomposites

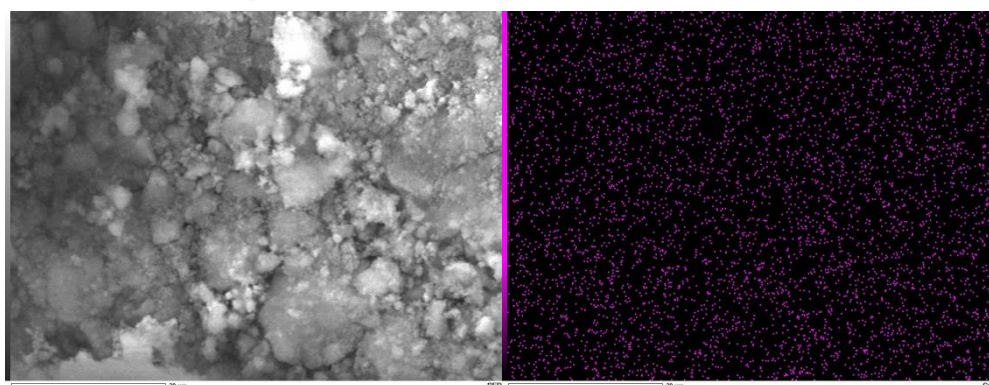


Figure 4.14 SEM images of the CuTCPP-TSI and the EDX elemental mapping for Cu element (pink spots)

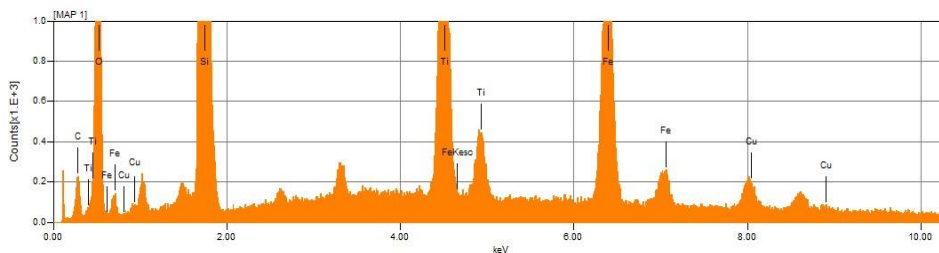


Figure 4.15 EDX spectra of CuTCPP-TSI composites

SEM images with EDX elemental mapping for Cu element were taken to determine the morphology of the CuTCPP-TSI sample and the effect of compositing on the displayed structure (Figure 4.14). Pink spots were identified to the area where Cu element signal was detected. This result demonstrated that Cu element could distribute well and showed no aggregation on specific area on CuTCPP-TSI surface.

Table 4.4 The elements in CuTCPP-TSI composites

Elements	Atom%
C	14.67
O	41.37
Si	24.24
Ti	9.32
Fe	8.78
Cu	1.63
Total	100

CuTCPP-TSI samples are composed of Fe, Si, Ti, O, C, and Cu in as-prepared products as seen in Figure 4.15 and Table 4.4. It was implied that Fe, Si, Ti, O, C, and Cu elements was the main composition in the CuTCPP-TSI nanocomposites. 1.63% Cu by mole in CuTCPP-TSI was calculated using this technique.

Table 4.5 The average particle sizes of TSI and CuTCPP-TSI determined using a dynamic light scattering (DLS) analysis.

Sample	Sizes (nm)	Polydispersity Index (PDI)
TSI	118.07±1.19	0.227±0.027
CuTCPP-TSI	134.53±2.89	0.183±0.030

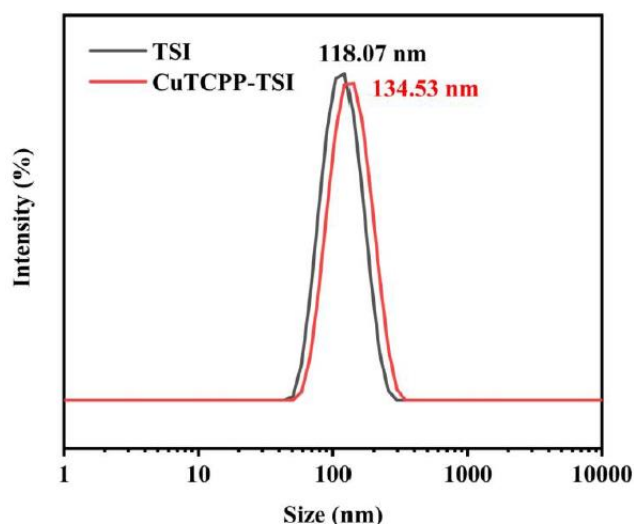


Figure 4.16 Hydrodynamic size distribution of TSI and CuTCPP-TSI dispersed in ethanol

Hydrodynamic sizes of the TSI nanocomposites and CuTCPP-TSI nanocomposites were calculated using a Malvern Zetasizer Nano ZSP. The dynamic light scattering (DLS) size measurements were investigated to estimate the stability of the nanocomposites when each composite was dispersed in PBS buffer pH 7.4 as dispersant.

The average hydrodynamic particle size of TSI nanoparticles was 118.07±1.19 nm with polydispersity index of 0.277±0.027. They demonstrated the nanosized particles without large aggregation (Table 4.5 and Figure 4.16). After these materials were attached with CuTCPP, a small increase in the hydrodynamic size of the nanocomposites was observed. The average hydrodynamic particle size of CuTCPP-TSI nanocomposites was 134.53±2.89 nm with polydispersity index about 0.183±0.03. A little increase in size can be implied that CuTCPP complexes were adsorbed on TSI surface. No signal of large aggregation was obtained in the dispersion of the composites during the measurement as seen from the size

distribution and hydrodynamic size of the composites. It could be foreseen that these nanocomposites could become homogeneous dispersion when they are applied as photocatalysts.

The estimated size from DLS analysis gave bigger sizes of particles than the measured size from TEM analysis in the same samples because the calculated sizes based on the speed of particles under Brownian motion for the DLS technique. Not only the size of the particles, but also type of dispersant, aggregation of particles, surface structure, and concentration of ions in the medium can affect to size from DLS. The hydrodynamic diameter, the layer around particles, was formed when the particles was dispersed in medium. Hence, the DLS data cannot be used for absolute size of particles, but only for indication of aggregation.

To determine the surface chemical composition and valence state of metal ion on metalloporphyrins before and after modification on TSI nanocomposite surface, the XPS spectra of various metals in the cavity of metalloporphyrins formed on TSI composite surface and the free metalloporphyrins were detected. As shown in Figure 4.17, the high resolution XPS spectra of Mn, Fe, Cu, and Zn were presented as MnTCPP and MnTCPP-TSI, FeTCPP and FeTCPP-TSI, CuTCPP and CuTCPP-TSI, ZnTCPP and ZnTCPP-TSI, respectively. The binding energies are carried out to provide details on the synthesized metalloporphyrin TSI composites. The Mn 2p XPS signal of MnTCPP and MnTCPP-TSI is shown in Figure 4.17a, two fitted peaks at the position of Mn ( $2p_{3/2}$ ) and Mn ( $2p_{1/2}$ ) transitions [36], usually corresponding to Mn(II), can be observed. While for FeTCPP and FeTCPP-TSI, two separate peaks located at 710.7 and 724.1 eV are due to the transitions of Fe ( $2p_{3/2}$ ) and Fe ( $2p_{1/2}$ ), respective. These binding energies are assigned to Fe(III), as previously reported [37]. For CuTCPP-TSI spectra, two peaks can be observed at 934.5 and 954.4 eV in the Cu 2p spectra corresponding to the Cu ( $2p_{3/2}$ ) and Cu ( $2p_{1/2}$ ) transitions, which are also confirmed the oxidation state of Cu(II) [25]. The Zn ( $2p_{3/2}$ ) peak and the Zn ( $2p_{1/2}$ ) peak of ZnTCPP in ZnTCPP-TSI composites appear at binding energies of 1021.9 and 1045.1 eV, respectively [38]. The Zn XPS spectra indicated the presence of Zn(II) in ZnTCPP-TSI nanocomposites. All the XPS results are evidence to confirm the presence of different metals [Cu(II), Mn(II), Fe(III), Zn(II)] on the metalloporphyrin composites, indicating that the valence state and the coordination of the metals on



metalloporphyrin molecules did not significantly change after the loading of metalloporphyrin complexes on to the TSI surface. XPS results not only supported the existence of metalloporphyrins on the titania surface, but also agreed well with the UV-vis absorption spectra results.

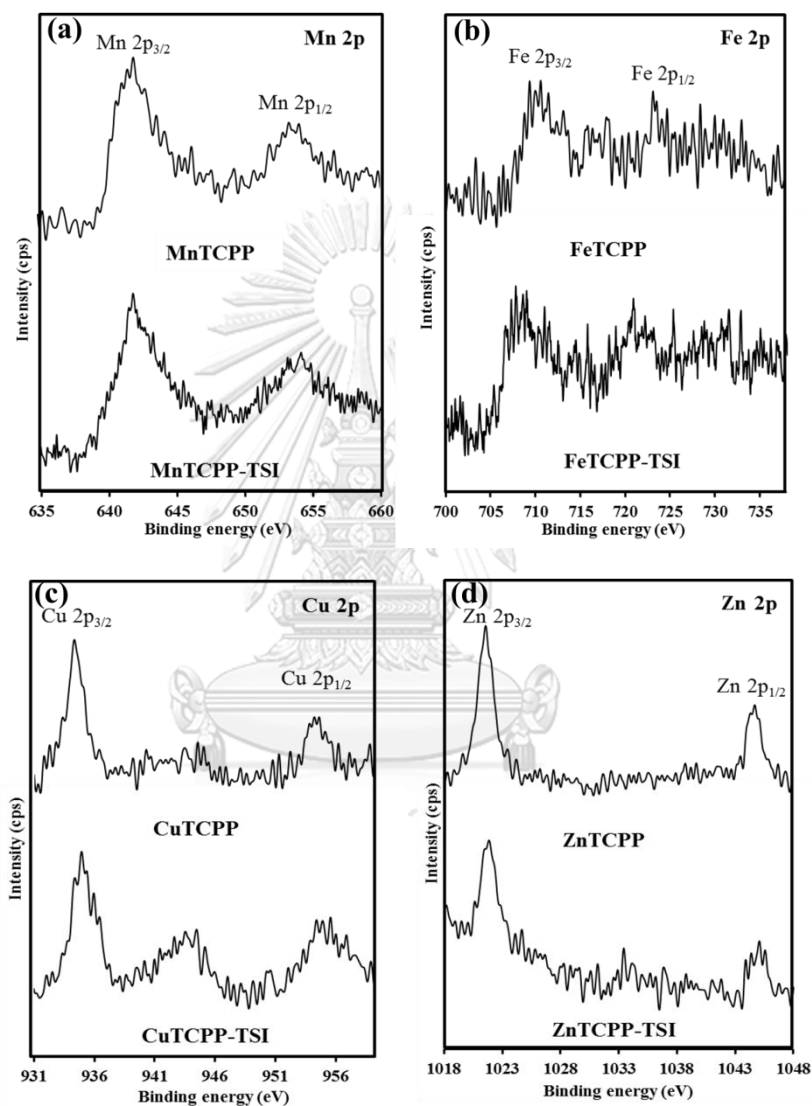


Figure 4.17 High-resolution XPS spectra of (a) Mn 2p of MnTCPP and MnTCPP-TSI, (b) Fe 2p of FeTCPP and FeTCPP-TSI, (c) Cu 2p of CuTCPP and CuTCPP-TSI, and (d) Zn 2p of ZnTCPP and ZnTCPP-TSI nanocomposites

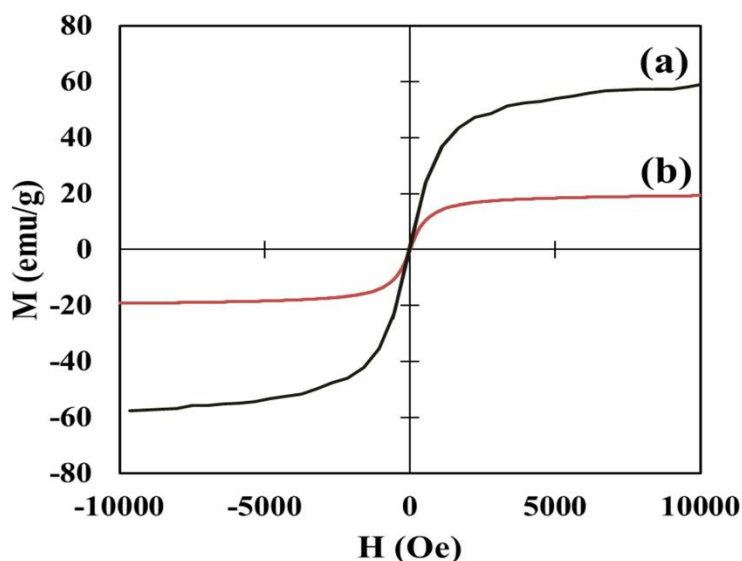


Figure 4.18 Magnetization curves obtained at room temperature of the (a) iron oxide nanoparticles (I), and (b) CuTCPP-TSI nanocomposites

The magnetic properties of the CuTCPP-TSI and iron oxide nanoparticles were characterized at room temperature using a vibrating sample magnetometer (VSM) as shown in Figure 4.18. It can be discerned that both magnetization curves showed superparamagnetic character at room temperature as no hysteresis phenomenon existed and no observable coercivity [8]. The saturation magnetization ( $M_s$ ) values were 58 emu/g and 19 emu/g for the iron oxide (I) magnetic nanoparticles with excess oleic acid surfactant and CuTCPP-TSI composites, respectively. After the coating process, the decrease in the  $M_s$  values of the CuTCPP-TSI was detected as expected owing to the addition of diamagnetic coatings, resulting in the increased diamagnetic contents in the nanocomposites.

To test the photodegradation performance of the TCPP, MTCPP with the different metal centers anchored on TSI surface toward the decrease in the absorbance of methylene blue (MB) as a model pollutant in aqueous medium under visible light irradiation were evaluated in comparison with TSI. As seen in Figure 4.19, the changes in MB during the degradation by TSI and MTCPP-TSI magnetic photocatalysts that contained TCPP with various metal centers and metal-free on the porphyrin indicated important differences in the photocatalytic efficiency. The best photocatalytic performance was observed with CuTCPP-TSI magnetic nanocomposite. After 3 h under irradiation, 98% of methylene blue (MB) was

degraded using CuTCPP-TSI. While in the same condition, TSI nanocomposites degraded only 2.9% of MB. Photocatalytic degradation rates of 58%, 36%, 29%, and 21% were found for ZnTCPP-TSI, MnTCPP-TSI, FeTCPP-TSI, and TCPP-TSI, respectively. When porphyrins were adsorbed on the TSI, all nanocomposites showed clearly enhanced photocatalytic activity compared to bare TSI composites. Increasing catalytic degradation activity in the order of CuTCPP-TSI > ZnTCPP-TSI > MnTCPP-TSI > FeTCPP-TSI > TCPP-TSI was exhibited.

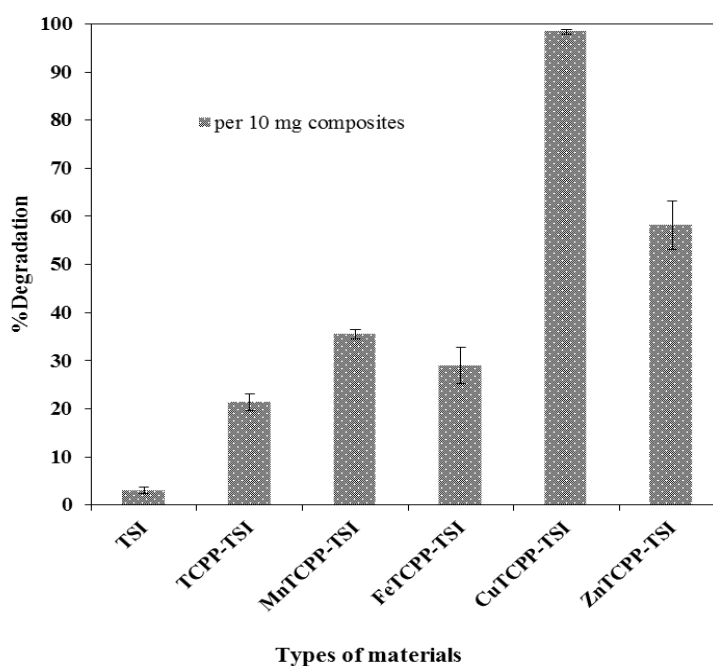


Figure 4.19 Photodegradation activity of methylene blue (MB) with 10 mg of each photocatalyst after 3h of irradiation

On the other hand, a little difference in the absorbance of different types of metalloporphyrins or free-metal porphyrin was obtained, suggesting that a little difference in weight ratio of the porphyrins anchored on TSI. The effect from the quantity of the porphyrins was eliminated to understand the influence of the type of metal centers on the photodegradation efficiency. The adsorbed percentage of porphyrins on TSI was measured using the absorbance at  $\lambda_{\max}$  of each porphyrin subtracted the background of TSI. For the same amount of porphyrin, the percentage of MB degradation within 3 h of irradiation per the loading of porphyrin in percentage attached on TSI nanocomposites was changed to 32%, 13%, 18%, 17% and 6% for

CuTCPP-TSI, ZnTCPP-TSI, MnTCPP-TSI, FeTCPP-TSI, and TCPP-TSI, respectively. Among different types of metal porphyrins, the photodegradation increased in the order of CuTCPP-TSI > MnTCPP-TSI, FeTCPP-TSI > ZnTCPP-TSI > TCPP-TSI based on the same loading percent of porphyrin on composites.

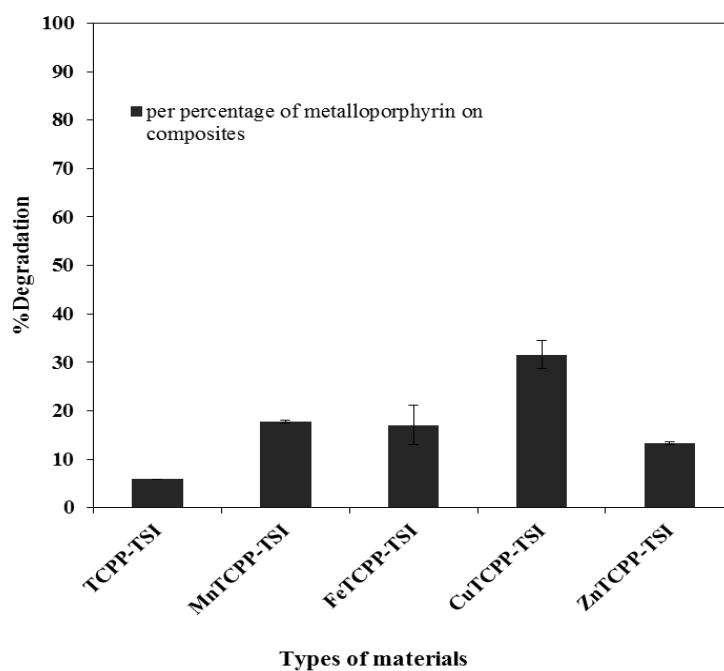


Figure 4.20 Photodegradation activity of methylene blue (MB) under 3h of irradiation with the same amount of porphyrin attached on TSI surface

When comparing in the same amount of porphyrin, the photocatalytic degradation results implied that the metalloporphyrin adsorbed on TSI could give a better photocatalytic activity than free-base porphyrin attached on TSI. We had tried to find the reasons for explaining these phenomena, and we found that their energy level as revealed in the Figure 4.21 could lead to different photocatalytic activity [39].

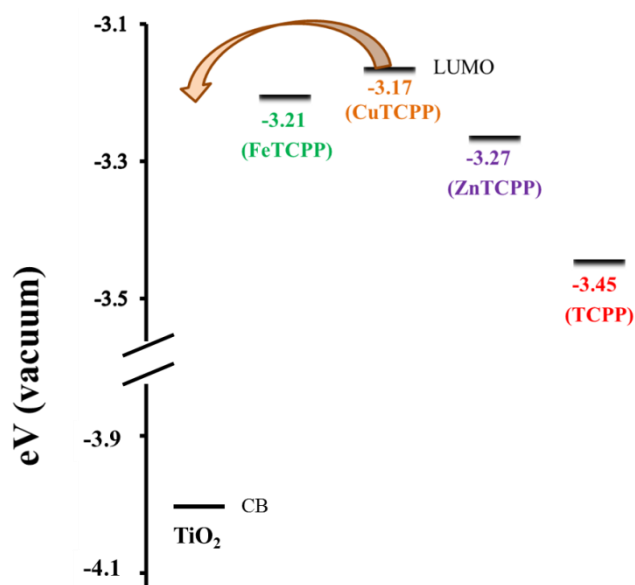
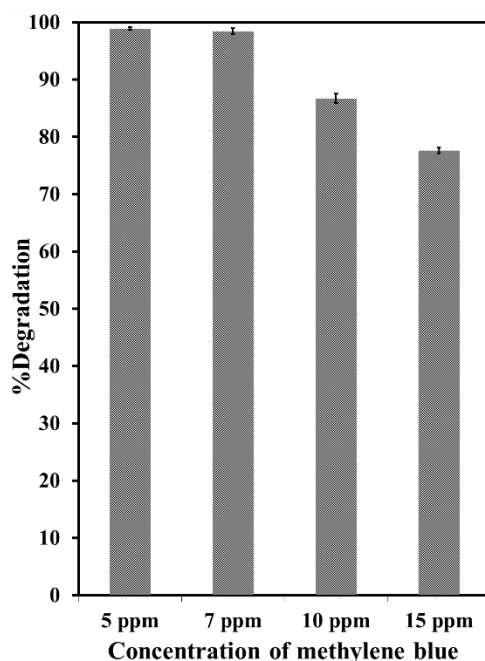


Figure 4.21 Energy level diagram of different metalloporphyrins and free-metal porphyrin compared to conduction band of titania on TSI composites [39]

This diagram can be described in terms of the electron transfer process from sensitizer (porphyrin) to the conduction band of titania upon irradiation. The behavior of all sensitizers based on the LUMO level: CuTCPP > FeTCPP > ZnTCPP > TCPP [39]. The higher in the LUMO level makes it easier for porphyrin to efficiently transfer electron after excitation toward to the conduction band of titania. Different metal centers on porphyrin demonstrated different electron injection driving force to transfer electrons to titania. Based on the diagram above, CuTCPP has the highest LUMO level, meaning that the driving force for the injection of excited electron to titania was larger than other metalloporphyrin. These electrons can then readily move to O<sub>2</sub> molecules, resulting in a multiplication in the radical species in the reaction solution [22, 39]. The presence of metal center in porphyrin cavity increases the electron transfer efficiency as compared to metal-free porphyrin. The above photocatalytic degradation results from MTCPP-TSI photocatalysts study reveals that the CuTCPP-TSI photocatalysts under visible irradiation exhibited highest photocatalytic efficiency in the degradation of MB due to its high energy LUMO level.



*Figure 4.22 At the different concentration of MB photodegradation upon 3 h of irradiation using CuTCPP-sensitized TSI nanocomposite (CuTCPP-TSI)*

The influence of initial concentration of MB on the photodegradation activity was investigated with a constant CuTCPP-TSI nanocomposites weight of 10 mg. Different MB concentrations ranging from 5 to 15 ppm were tested. 30 mL of MB solution was fixed within 3 h of irradiation. The trend for photodegradation efficiency decreased when an initial concentration of MB was increased as seen in Figure 4.22. Because the methylene blue concentration was increased, but the loading of the nanocomposites dispersed in methylene blue solution still remained the same. At high concentration of MB, the amounts of generated radicals from the composites were not high enough to degrade high amount of MB, leading to the reduction in MB photodegradation activity. Besides, the visible light penetrated less through high concentration of MB solution, resulting in the decrease in the amount of radicals formed. Consequently, the photocatalytic efficiency reduced upon increasing MB concentration.

#### 4.2.2 The effect of the different anchoring group on the photocatalytic performance

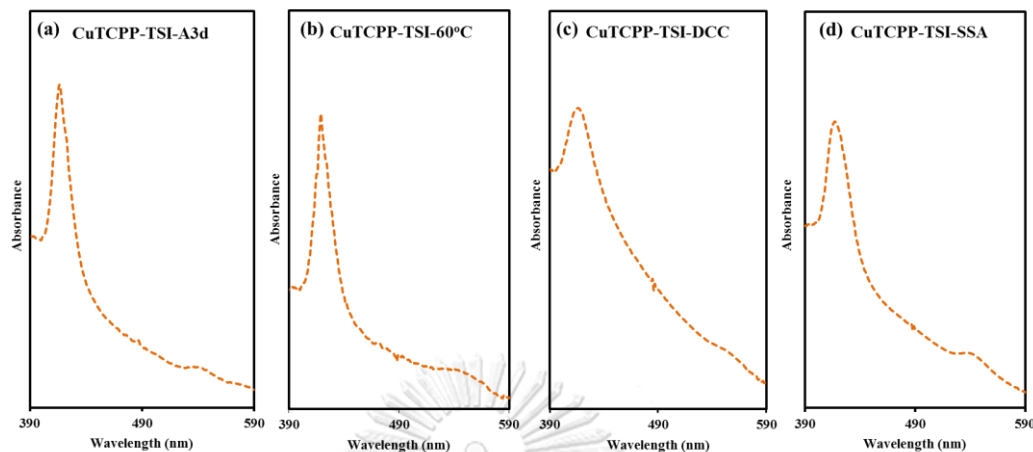


Figure 4.23 The UV-Vis spectra of CuTCPP-TSI samples with the different synthesized method (a) adsorption for 3 days, (b) stirring at 60 °C, (c) DCC coupling, (d) SSA as bridging molecule

For the investigation of the effect of anchoring group of porphyrins and titania, all CuTCPP-TSI spectra showed the red shift of absorbance compared to that in the absorption spectrum of CuTCPP (Figure 4.23). It can confirm that CuTCPP has been successfully attached on the composite surface with some strong interaction.

Table 4.6 The percentage of nitrogen in TSI and TSI-NH<sub>2</sub> from CHSN elemental analysis

Samples	%N
TSI	0.59
TSI-NH <sub>2</sub>	3.08

The attachment of amine groups on TSI surface was confirmed using the CHON analysis. %N in TSI composites and TSI-NH<sub>2</sub> composites were 0.59 and 3.08, respectively. After APTES were conjugated on TSI surface, %N in TSI-NH<sub>2</sub> sample increased, which can indicate the successful synthesis for changing the functional group from -OH to be -NH<sub>2</sub> group.

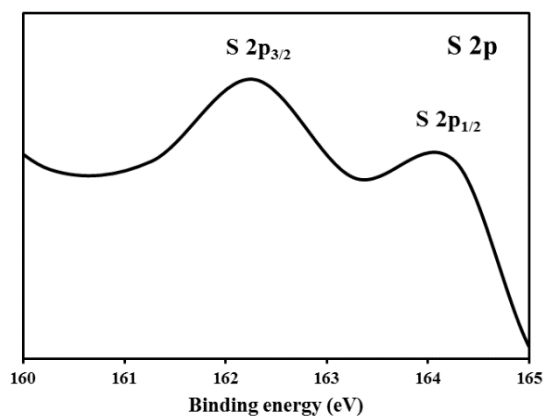


Figure 4.24 XPS spectrum of S 2p in CuTCCP-TSI-SSA sample

To confirm the binding between the TSI and SSA, the XPS spectrum of S 2p can be found as two peaks at S 2p<sub>3/2</sub> and S 2p<sub>1/2</sub> [38]. It can confirm the presence of S in SSA as bridging molecule for CuTCCP-TSI-SSA product. This result showed the success in the preparation using SSA as bridging molecule.

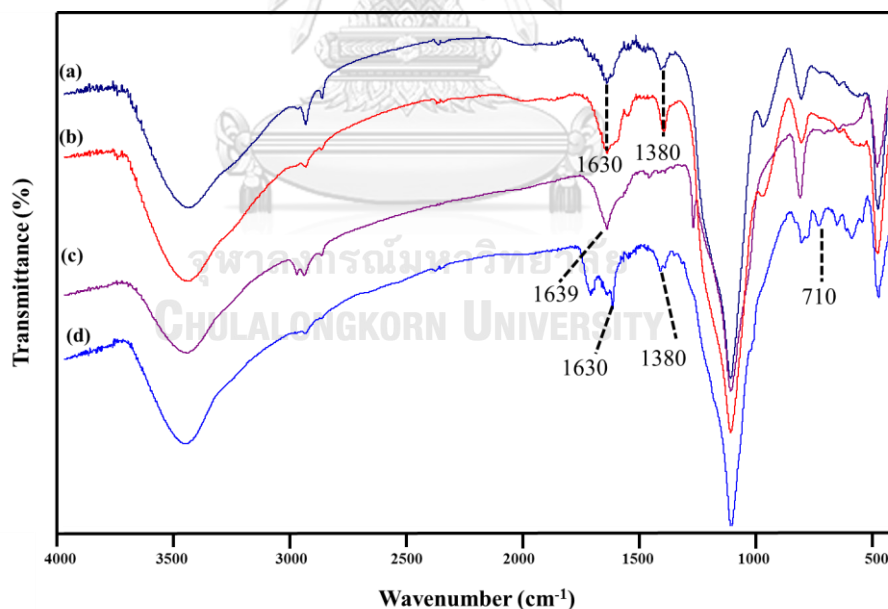
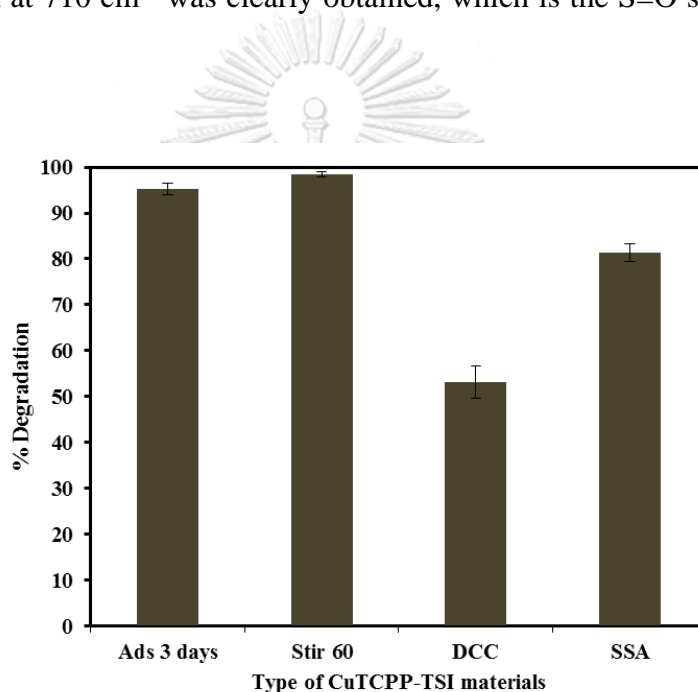


Figure 4.25 FT-IR of CuTCCP-TSI samples with the different synthesized method (a) adsorption for 3 days, (b) stirring at 60 °C, (c) DCC coupling, (d) SSA as bridging molecule

FT-IR results of CuTCCP-TSI samples with the different synthesized method are compared in Figure 4.25. Both of CuTCCP-TSI using adsorption for 3 days



(CuTCPP-TSI-A3d) and using stirring at 60 °C (CuTCPP-TSI-60 °C) were observed two new peak at 1630 (overlap with the O-H bending vibration) and 1380  $\text{cm}^{-1}$ , which indicated that the adsorption of carboxylate group in CuTCPP to the  $\text{TiO}_2$  [19, 26]. The FT-IR spectrum of CuTCPP-TSI using DCC coupling showed that 1639  $\text{cm}^{-1}$ , which was attributed to the C=O stretching of amide bond between the carboxylic group of CuTCPP and the amine group of the modified TSI with APTES group (TSI-NH<sub>2</sub> composites) [23]. The presence of both the symmetric and asymmetric stretching of  $-\text{COO}^-$  at 1630 and 1380  $\text{cm}^{-1}$ , revealing that CuTCPP was bound using ester bond [19]. The peak at 710  $\text{cm}^{-1}$  was clearly obtained, which is the S=O stretching of SSA [19].



*Figure 4.26 Photodegradation activity of methylene blue (MB) under 3h of irradiation based on the same amount of catalysts with different anchoring groups*

For the investigation of the effect of anchoring group of porphyrins and titania on the MB photodegradation, the photocatalytic activity of all CuTCPP-TSI with the different anchoring groups based on the same amount of catalyst: CuTCPP-TSI-60°C, CuTCPP-TSI-A3d > CuTCPP-TSI-SSA > CuTCPP-TSI-DCC (Figure 4.26). The photodegradation was 98.4%, 95.3%, 81.4%, and 53.1% for CuTCPP-TSI-60°C, CuTCPP-TSI-A3d, CuTCPP-TSI-SSA and CuTCPP-TSI-DCC, respectively.

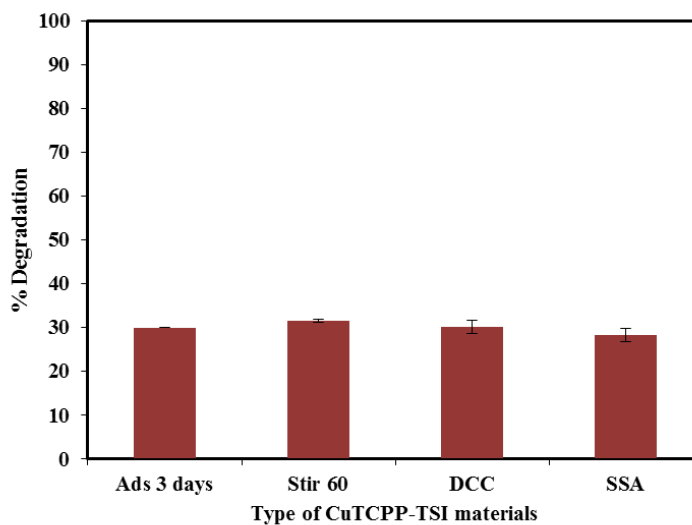


*Figure 4.27 Photodegradation activity of methylene blue (MB) under 3h of irradiation based on the same amount of porphyrin attached on CuTCPP-TSI surface with the different anchoring group*

For the same amount of porphyrin (Figure 4.27), the percentage of degradation MB within 3 h of irradiation per percentage of CuTCPP attached on TSI nanocomposites with different anchoring group showed that no signification in the effect of different anchoring group. Therefore, it is not the approach of attachment, but the amount of CuTCPP on the materials is an important factor on the photodegradation.

#### 4.2.3 Reusability of the nanocomposites

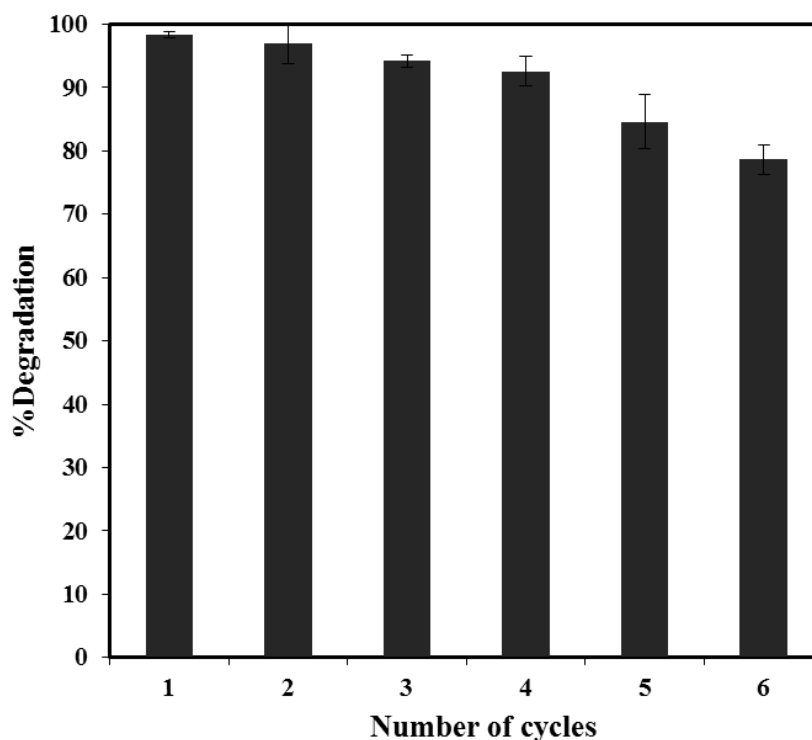


*Figure 4.28 The photodegradation of methylene blue upon visible light irradiation using CuT CPP-TSI nanocomposite (CuT CPP-TSI) in different cycles of reused CuT CPP-TSI.*

The reusability of CuT CPP-TSI nanocomposites was investigated by magnetic separation after completing photocatalytic degradation. These composites were easily separated out from the reaction mixture. The photodegradation experiment of methylene blue was investigated repeatedly for four times under the same experimental condition. In each cycle of reused nanocomposites, they were done without regeneration process. Only a small reduction in photodegradation activity was observed, and the catalysts remained as high efficiency after four cycles as shown in Figure 4.28. Observably, the photocatalytic efficiency of the CuT CPP-TSI nanocomposites revealed that percentage of degradation did not significantly decrease after several reaction cycles without catalyst regeneration. After used for four times, the MB was decomposed with only a small change on photooxidation activity by CuT CPP-TSI nanocomposites likely owing to the incomplete decomposition in previous photooxidation reaction that can lead to some deposition of by-products onto the CuT CPP-TSI nanocomposite surface.

The leaching of copper ions was obtained using the inductively coupled plasma-optical emission spectrometer (ICP-OES). A very small leaching occurred in the MB solution during the photodegradation reaction. The average concentration was about 5 ppb copper ions in the solution after photodegradation, so only a small leaching was observed, indicating that this material can be used as a photocatalyst with minimal contamination.

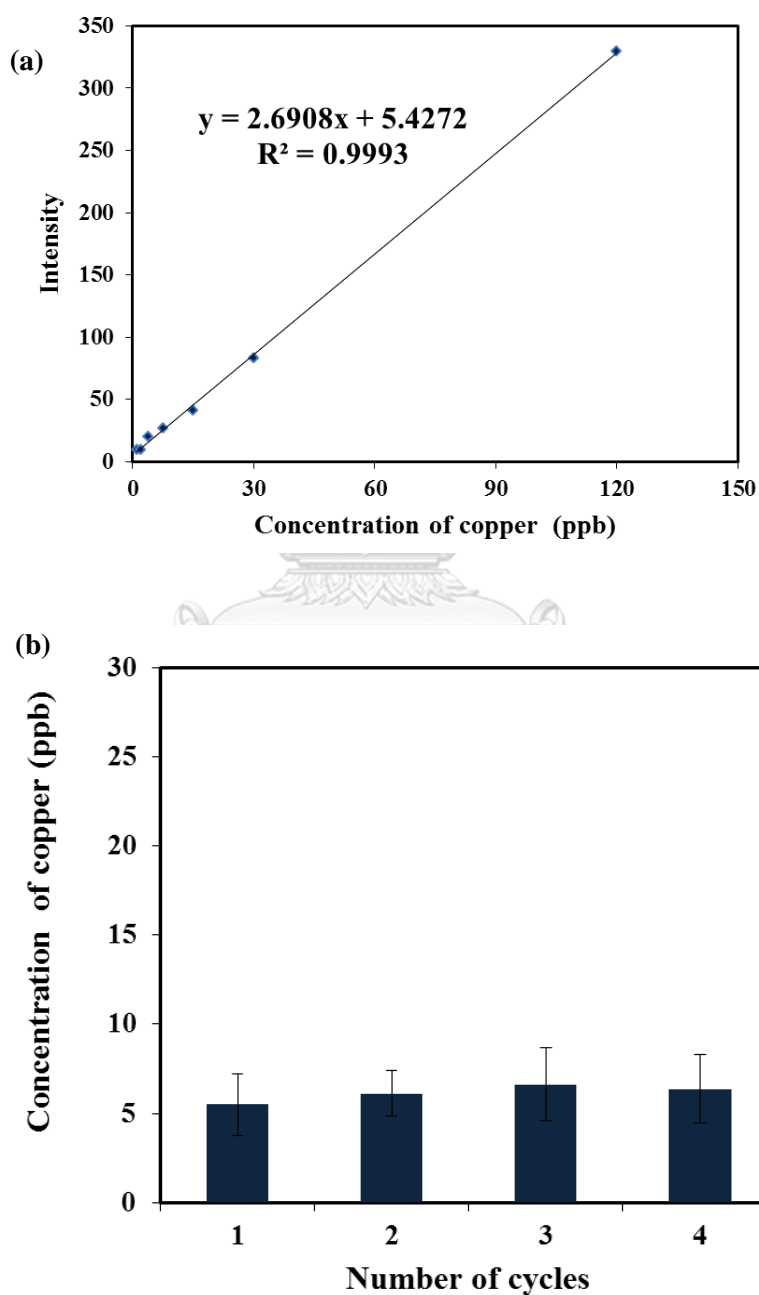


Figure 4.29 (a) The standard calibration curve of copper ion and (b) The concentration of copper ion in the MB solution after photodegradation reaction

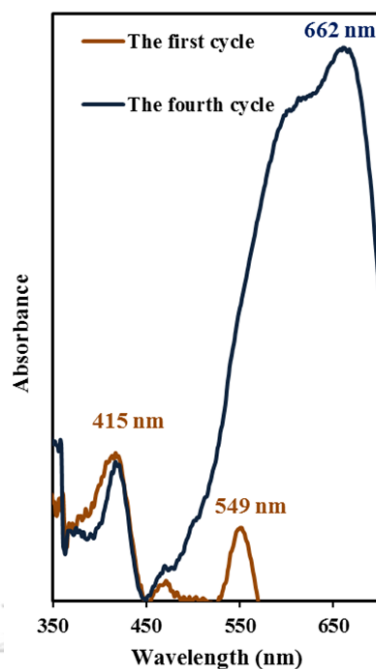


Figure 4.30 Diffuse reflectance UV-vis absorption spectra of CuTCPP-TSI before the photooxidation reaction of MB solution and after the fourth cycle of reuse.

Diffuse reflectance Ultraviolet-visible absorption spectra of the CuTCPP-TSI before oxidation reaction and after reaction for four cycles are shown in Figure 4.30. The diffuse reflectance UV-vis absorption spectrum of CuTCPP-TSI exhibited the Soret band and Q band of CuTCPP on the composite surface in case of fresh materials. After used for four times, the diffuse reflectance UV-vis absorption spectrum of CuTCPP-TSI remained the Soret band at around that 415 nm was correlated with the fresh one, indicating that the CuTCPP was adsorbed on the TSI with high stability for the photooxidative reaction. In addition, a new broad band at around 662 nm which obscured the Q band of CuTCPP was observed in the catalyst after photodegradation, which is likely due to the methylene blue residues. It is in agreement with the hypothesis that the reduction of photooxidative activity in the nanocomposites is due to the surface deactivated by residue adsorption.

### 4.3 Antibacterial activity

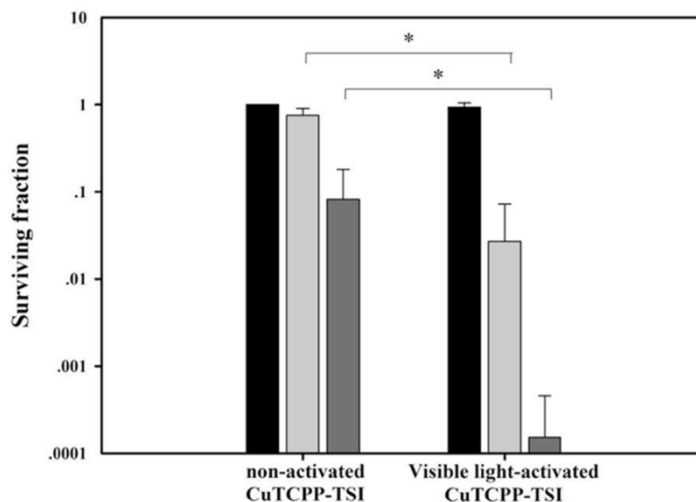


Figure 4.31 The bactericidal activity with non-activated and visible-light-activated CuTCPP-TSI nanocomposites at 0 mg/L (black bar), 17.5 mg/L (light gray bar) and 20.0 mg/L (dark gray bar) within 3 h of irradiation. The asterisk (\*) revealed statistically different ( $p$ -value < 0.05, paired  $t$ -test).

Gram negative *E. coli* was chosen as a testing model for our work. The CuTCPP-TSI nanocomposites were evaluated for the bactericidal activity using previously described procedures [4]. Some previous articles reports that titania particles can produce reactive oxygen radicals such as superoxide anions and hydroxyl radicals [24, 40-43]. These radicals are able to damage biomolecules of bacteria, leading to cell death. Thus, the reactive oxygen radicals generated by the irradiated CuTCPP-TSI nanocomposites could provide stress to bacteria and cause bacterial cell death.

The light activated CuTCPP-TSI nanocomposites were able to degrade methylene blue as seen in photocatalytic activity (Section 4.2), confirming that some radicals were produced by these materials. The bacterial cells were treated by the visible light activated with various concentrations of CuTCPP-TSI nanocomposites compared to non-light activated CuTCPP-TSI nanocomposites. Control experiment was done as the same condition as the treated with CuTCPP-TSI composites except adding of CuTCPP-TSI. The antibacterial results displayed that the CuTCPP-TSI nanocomposite with visible light activation could efficiently kill the bacterial cells. More than 99.9% of the bacterial cells were killed by 20.0 mg/L of CuTCPP-TSI

nanocomposites, whereas the 17.5 mg/L of nanocomposite concentration can dramatically kill the bacterial cells. The antibacterial activity of these light-activated catalysts was depended on concentration. Moreover, the non-activated CuTCPP-TSI nanocomposite also showed a small antibacterial activity because these nanocomposites consist of copper metal. This transition metal is a toxic substance for the bacteria. As the result seen in Figure 4.32, the bacterial killing property exhibits more effectively with the activation of nanocomposites under visible irradiation.

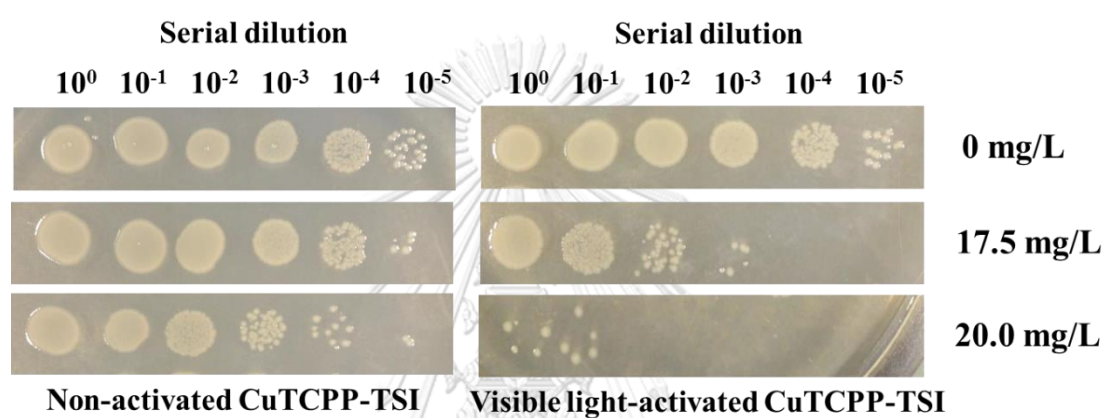


Figure 4.32 The antibacterial activity of CuTCPP-TSI against *E. coli*.

## CHAPTER V

### CONCLUSION

Given the promising applications, the visible light active magnetic photocatalysts (MTCPP-sensitized TSI nanocomposites) exhibited both high photooxidative properties and magnetic response. They have been successfully synthesized using the thermal decomposition method for iron oxide core, followed by silica and anatase titania coating *via* a two-step reverse microemulsion technique. Meso-tetra(4-carboxyphenyl)porphyrin (TCPP) containing various metal centers [Mn(II), Fe(III), Cu(II), Zn(II), metal-free] were used to examine the most suitable metalloporphyrin for making the better visible-light active catalysts. All the obtained nanocomposites in this work were characterized using UV-visible spectroscopy, transmission electron microscopy (TEM), X-ray powder diffraction (XRD), Fourier transforms infrared spectroscopy (FT-IR), and X-ray photoelectron spectroscopy (XPS). The photocatalytic properties were investigated by the decrease in the concentration of methylene blue (MB) under visible light irradiation. For the study of the various metalloporphyrin attached on TSI nanocomposites for the photocatalytic performance, more than 98% of MB solution (7 ppm, 30 mL) was efficiently degraded by the CuTCPP-TSI nanocomposites within 3 h of irradiation. The CuTCPP-TSI nanocomposites showed the best performance compared to the other metalloporphyrins likely due to the more favorable electrons transportation to the conduction band of TiO<sub>2</sub> on CuTCPP-TSI composites. Besides, we were interested in the interaction between the porphyrin and TSI composites, and the results indicated that anchoring groups were insignificant when the same quantity of porphyrins was attached on TSI. The important factor for improving the photocatalytic property is the loading of porphyrin on the composite surface and type of metal center in the porphyrin cavity. These materials can be utilized to degrade methylene blue solution under visible irradiation for at least four times without any regeneration. Moreover, the CuTCPP-TSI nanocomposites were activated by the visible light for antibacterial



application. 99.9% of *E. coli* cells were killed with these photocatalysts upon the composite concentration 20.0 mg/L with 3 h of irradiation.

Finally, CuTCPP-TSI nanocomposites are possibly beneficial in organic pollutant degradation application and the bacterial eradication under the sunlight. The easy separation of these materials would lead to the many applications in the future.



## REFERENCES

- [1] Fujishima, A., Rao, T.N., and Tryk, D.A. Titanium Dioxide Photocatalysis. J. Photochem. Photobio., C 1 (2000): 1-21.
- [2] Schneider, J., et al. Understanding TiO<sub>2</sub> Photocatalysis: Mechanisms and Materials. Chem. Rev. 114 (2014): 9919-9986.
- [3] Beydoun, D., Amal, R., Low, G., and McEvoy, S. Novel Photocatalyst: Titania-Coated Magnetite. Activity and Photodissolution. J. Phys. Chem. 104 (2000): 4387-4396.
- [4] Chanhom, P., Charoenlap, N., Tomapatnaget, B., and Insin, N. Colloidal Titania-Silica-Iron Oxide Nanocomposites and the Effect from Silica Thickness on the Photocatalytic and Bactericidal Activities. J. Magn. Magn. Mater. 427 (2017): 54-59.
- [5] Pelaez, M., et al. A Review on the Visible Light Active Titanium Dioxide Photocatalysts for Environmental Applications. Appl. Catal., B: Environ. 125 (2012): 331-349.
- [6] Pirkanniemi, K. and Sillanpää, M. Heterogeneous Water Phase Catalysis as an Environmental Application: a Review. Chemosphere 48 (2002): 1047-1060.
- [7] Houas, A., Lachheb, H., Ksibi, M., Elaloui, E., Guillard, C., and Herrmann, J.-M. Photocatalytic Degradation Pathway of Methylene Blue in Water. Appl. Catal., B: Environ. 31 (2001): 145-157.
- [8] Pankhurst, Q.A., Connolly, J., Jones, S.K., and Dobson, J. Applications of Magnetic Nanoparticles in Biomedicine. J. Phys. D: Appl. Phys. 36 (2003): R167-R181.
- [9] Lu, A.-H., Salabas, E.L., and Schüth, F. Magnetic Nanoparticles: Synthesis, Protection, Functionalization, and Application. Angew. Chem. Int. Ed. 46 (2007): 1222-1244.
- [10] Park, J., et al. Ultra-Large-Scale Syntheses of Monodisperse Nanocrystals. Nat. Mater. 3 (2004): 891-895.
- [11] Gupta, A.K. and Gupta, M. Synthesis and Surface Engineering of Iron Oxide Nanoparticles for Biomedical Applications. Biomaterials 26 (2005): 3995-4021.
- [12] Chen, X. and Mao, S.S. Titanium Dioxide Nanomaterials: Synthesis, Properties, Modifications, and Applications. Chem. Rev. 107 (2007): 2891-2959.
- [13] Ding, H.L., Zhang, Y.X., Wang, S., Xu, J.M., Xu, S.C., and Li, G.H. Fe<sub>3</sub>O<sub>4</sub>@SiO<sub>2</sub> Core/Shell Nanoparticles: The Silica Coating Regulations with a Single Core for Different Core Sizes and Shell Thicknesses. Chem. Mater. 24 (2012): 4572-4580.
- [14] Zhang, D., Qi, L., Ma, J., and Cheng, H. Formation of Crystalline Nanosized Titania in Reverse Micelles at Room Temperature. J. Mater. Chem. (2002): 3677-3680.
- [15] Li, L.-L. and Diau, E.W. Porphyrin-Sensitized Solar Cells. Chem. Soc. Rev. 42 (2013): 291-304.
- [16] Valicsek, Z. and Horváth, O. Application of the Electronic Spectra of Porphyrins for Analytical Purposes: The Effects of Metal Ions and Structural Distortions. Microchem. J. 107 (2013): 47-62.
- [17] Cabeen, M.T. and Wagner, C.J. Bacterial Cell Shape. Nat. Rev. Microbiol. 3 (2005): 601-610.

- [18] Beydoun, D., Amal, R., Low, G., and McEvoy, S. Occurrence and Prevention of Photodissolution at the Phase Junction of Magnetite and Titanium Dioxide. J. Mol. Catal., A: Chem. 180 (2002): 193–200.
- [19] Yao, B., Peng, C., Zhang, W., Zhang, Q., Niu, J., and Zhao, J. A Novel Fe(III) Porphyrin-Conjugated TiO<sub>2</sub> Visible-Light Photocatalyst. Appl. Catal., B: Environ. 174-175 (2015): 77-84.
- [20] Afzal, S., Daoud, W.A., and Langford, S.J. Photostable Self-Cleaning Cotton by a Copper(II) Porphyrin/TiO<sub>2</sub> Visible-Light Photocatalytic System. ACS Appl. Mater. Interfaces 5 (2013): 4753–4759.
- [21] Cai, J.H., Huang, J.W., Yu, H.C., and Ji, L.N. Synthesis, Characterization, and Photocatalytic Activity of TiO<sub>2</sub> Microspheres Functionalized with Porphyrin. Int. J. Photoenergy 2012 (2012): article ID 348292.
- [22] Granados-Oliveros, G., Páez-Mozo, E.A., Ortega, F.M., Ferronato, C., and Chovelon, J.-M. Degradation of Atrazine Using Metalloporphyrins Supported on TiO<sub>2</sub> under Visible Light Irradiation. Appl. Catal. B: Environ. 89 (2009): 448-454.
- [23] Rahimi, R., Moghaddas, M.M., and Zargari, S. Investigation of the Anchoring Silane Coupling Reagent Effect in Porphyrin Sensitized Mesoporous V-TiO<sub>2</sub> on the Photodegradation Efficiency of Methyl Orange under Visible Light Irradiation. J. Sol-Gel Sci. Technol. 65 (2013): 420-429.
- [24] Sunada, K., Watanabe, T., and Hashimoto, K. Studies on Photokilling of Bacteria on TiO<sub>2</sub> Thin Film. J. Photochem. Photobiol. A: Chem. 156 (2003): 227-233.
- [25] Pham, T.-D. and Lee, B.-K. Cu Doped TiO<sub>2</sub>/GF for Photocatalytic Disinfection of *Escherichia coli* in Bioaerosols under Visible Light Irradiation: Application and Mechanism. Appl. Surf. Sci. 296 (2014): 15-23.
- [26] Zargari, S., Rahimi, R., and Yousefi, A. An Efficient Visible Light Photocatalyst Based on Tin Porphyrin Intercalated Between TiO<sub>2</sub>-Graphene Nanosheets for Inactivation of *E. coli* and Investigation of Charge Transfer Mechanism. RSC Adv. 6 (2016): 24218-24228.
- [27] Zhao, X., Liu, X., Yu, M., Wang, C., and Ji, J. The Highly Efficient and Stable Cu, Co, Zn-Porphyrin-TiO<sub>2</sub> Photocatalysts with Heterojunction by using Fashioned One-Step Method. Dyes Pigments 136 (2017): 648-656.
- [28] Granados-Oliveros, G., et al. Visible Light Production of Superoxide Anion with M-carboxyphenylporphyrins (M=H, Fe, Co, Ni, Cu, and Zn) Free and Anchored on TiO<sub>2</sub>: EPR Characterization. J. Mol. Catal. A: Chem. 339 (2011): 79-85.
- [29] Chanhom, P., Charoenlap, N., Manipuntee, C., and Insin, N. Metalloporphyrins-Sensitized Titania-Silica-Iron Oxide Nanocomposites with High Photocatalytic and Bactericidal Activities under Visible Light Irradiation. J. Magn. Magn. Mater. 475 (2019): 602-610.
- [30] Poursaberi, T., Akbar, V., Shoja, S., and Seyed, M.R. Application of Rh(III)-Metalloporphyrin Grafted Fe<sub>3</sub>O<sub>4</sub> Nanoparticles for the Extraction of Thiocyanate Ions from Aqueous Solutions. Iran. J. Chem. Eng. 34 (2015): 41-49.
- [31] Prapagdee, B., Vattanaviboon, P., and Mongkolsuk, S. The Role of a Bifunctional Catalase-Peroxidase KatA in Protection of *Agrobacterium Tumefaciens* from Menadione Toxicity. FEMS Microbiol. Lett. 232 (2004): 217–223.

- [32] Rabbani, M., Bathaee, H., Rahimi, R., and Maleki, A. Photocatalytic Degradation of p-Nitrophenol and Methylene Blue using Zn-TCPP/Ag Doped Mesoporous TiO<sub>2</sub> under UV and Visible Light Irradiation. Desalin. Water Treat. (2016): 1-9.
- [33] Dehkordi, L.H. and Monfared, H.H. Enantioselective Aerobic Oxidation of Olefins by Magnetite Nanoparticles at Room Temperature: a Chiral Carboxylic Acid Strategy. Green Chem. 18 (2016): 497-507.
- [34] Nakashima, S., Negishi, R., and Tada, H. Visible-Light-Induced Water Oxidation by a Hybrid Photocatalyst Consisting of Bismuth Vanadate and Copper(II) meso-Tetra(4-Carboxyphenyl)Porphyrin. Chem. Commun. 52 (2016): 3665-3668.
- [35] Rahimi, R., Saadati, S., and Fard, E.H. Fluorine-Doped TiO<sub>2</sub> Nanoparticles Sensitized by Tetra(4-Carboxyphenyl)Porphyrin and Zinc Tetra(4-Carboxyphenyl)Porphyrin: Preparation, Characterization, and Evaluation of Photocatalytic Activity. Environ. Prog. Sustain. 34 (2015): 1341-1348.
- [36] Farokhi, A. and Monfared, H.H. A Recyclable Mn-porphyrin Catalyst for Enantioselective Epoxidation of Unfunctionalized Olefins using Molecular Dioxygen. New J. Chem. 40 (2016): 5032-5043.
- [37] Wei, M., Wan, J., Hu, Z., Peng, Z., Wang, B., and Wang, H. Preparation, Characterization and Visible-Light-Driven Photocatalytic Activity of a Novel Fe(III) Porphyrin-Sensitized TiO<sub>2</sub> Nanotube Photocatalyst. Appl. Surf. Sci. 391 (2017): 267-274.
- [38] Yuan, Y.-J., et al. Visible-Light-Driven Hydrogen Production from Water in a Noble-Metal-Free System Catalyzed by Zinc Porphyrin Sensitized MoS<sub>2</sub>/ZnO. Dyes Pigments 123 (2015): 285-292.
- [39] Sehgal, P. and Narula, A.K. Metal Substituted Metalloporphyrins as Efficient Photosensitizers for Enhanced Solar Energy Conversion. J. Photochem. Photobiol., A: Chem. 375 (2019): 91-99.
- [40] Yemmireddy, V.K. and Hung, Y.C. Selection of Photocatalytic Bactericidal Titanium Dioxide (TiO<sub>2</sub>) Nanoparticles for Food Safety Applications. LWT-Food Sci. Technol. 61 (2015): 1-6.
- [41] Zhang, Z., Liu, H., Xu, J., and Zhang, N. Enhancing the Visible Light Absorption and Charge Separation of Bi<sub>2</sub>WO<sub>3</sub> by Hybridizing a CuTCPP Sensitizer. Photochem. Photobiol. Sci. 16 (2017): 1194-1200.
- [42] Kim, S., et al. Bacterial Inactivation in Water, DNA Strand Breaking, and Membrane Damage Induced by Ultraviolet-Assisted Titanium Dioxide Photocatalysis. Water Res. 47 (2013): 4403-4411.
- [43] Kühn, K.P., et al. Disinfection of Surfaces by Photocatalytic Oxidation with Titanium Dioxide and UVA Light. Chemosphere 53 (2003): 71-77.



จุฬาลงกรณ์มหาวิทยาลัย  
**CHULALONGKORN UNIVERSITY**

## VITA

**NAME** Padtaraporn Chanhom

**DATE OF BIRTH** 20 March 1988

**PLACE OF BIRTH** Ratchaburi, Thailand

**INSTITUTIONS ATTENDED** Bachelor Degree of Science in Chemistry, Silpakorn University, Nakhonpsthom, Thailand.  
Master Degree of Science in Inorganic Chemistry, Chulalongkorn University, Bangkok, Thailand.  
Doctoral Degree of Science in Inorganic Chemistry, Chulalongkorn University, Bangkok, Thailand.

**HOME ADDRESS** 98 Moo 5, Tanad, Damnoensaduak, Ratchaburi, Thailand

**PUBLICATION** Chanhom, P.; Charoenlap, N.; Tomapatnaget, B.; Insin, N. "Colloidal Titania-Silica-Iron Oxide Nanocomposites and the Effect from Silica Thickness on the Photocatalytic and Bactericidal Activities" *J. Magn. Magn. Mater.* 2017, 427, 54–59.  
Chanhom, P.; Charoenlap, N.; Manipuntee, C.; Insin, N. "Metalloporphyrins-sensitized titania-silica-iron oxide nanocomposites with high photocatalytic and bactericidal activities under visible light irradiation" *J. Magn. Magn. Mater.* 2019, 475, 602–610.